J. Fluid Mech. (2018), *vol.* 838, *pp.* 68–104.
doi:10.1017/jfm.2017.865

The common mechanism of turbulent skin-friction drag reduction with superhydrophobic longitudinal microgrooves and riblets

Amirreza Rastegari[1] **and Rayhaneh Akhavan**[1,†]

[1]Department of Mechanical Engineering, The University of Michigan, Ann Arbor, MI 48109-2125, USA

(Received 12 January 2017; revised 12 November 2017; accepted 26 November 2017; first published online 10 January 2018)

Turbulent skin-friction drag reduction with superhydrophobic (SH) longitudinal microgrooves and riblets is investigated by direct numerical simulation (DNS), using lattice Boltzmann methods, in channel flow. The liquid/gas interfaces in the SH longitudinal microgrooves were modelled as stationary, curved, shear-free boundaries, with the meniscus shape determined from the solution of the Young–Laplace equation. Interface protrusion angles of $\theta = 0°$, $-30°$, $-60°$, $-90°$ were investigated. For comparison, the same geometries as those formed by the SH interfaces were also studied as riblets. Drag reductions of up to 61 % and up to 5 % were realized in DNS with SH longitudinal microgrooves and riblets, respectively, in turbulent channel flows at bulk Reynolds numbers of $Re_b = 3600$ ($Re_{\tau_0} \approx 222$) and $Re_b = 7860$ ($Re_{\tau_0} \approx 442$), with arrays of SH longitudinal microgrooves or riblets of size $14 \lesssim g^{+0} \lesssim 56$ and $g^{+0}/w^{+0} = 7$ on both walls, where g^{+0} and w^{+0} denote the widths and spacings of the microgrooves in base flow wall units, respectively. An exact analytical expression is derived which allows the net drag reduction in laminar or turbulent channel flow with any SH or no-slip wall micro-texture to be decomposed into contributions from: (i) the effective slip velocity at the wall, (ii) modifications to the normalized structure of turbulent Reynolds shear stresses due to the presence of this effective slip velocity at the wall, (iii) other modifications to the normalized structure of turbulent Reynolds shear stresses due to the presence of the wall micro-texture, (iv) modifications to the normalized structure of mean flow shear stresses due to the presence of the wall micro-texture and (v) the fraction of the flow rate through the wall micro-texture. Comparison to DNS results shows that SH longitudinal microgrooves and riblets share a common mechanism of drag reduction in which 100 % of the drag reduction arises from effects (i) and (ii). The contributions from (iii)–(v) were always drag enhancing, and followed a common scaling with SH longitudinal microgrooves and riblets when expressed as a function of the square root of the microgroove cross-sectional area in wall units. Extrapolation of drag reduction data from DNS to high Reynolds number flows of practical interest is discussed. It is shown that, for a given geometry and size of the surface micro-texture in wall units, the drag reduction performance of micro-textured surfaces degrades with increasing bulk Reynolds number of the flow. Curved SH interfaces at low protrusion angle ($\theta = -30°$) were found to enhance the drag reduction by up to 3.6 % compared to flat interfaces, while reducing the instantaneous pressure fluctuations on the SH interfaces by up to a factor of two.

† Email address for correspondence: raa@umich.edu

This suggests that the longevity of SH interfaces in turbulent flow may be improved by embedding the SH surface within the microgrooves of shallow, scalloped riblets.

Key words: drag reduction, micro-/nano-fluid dynamics, turbulence control

1. Introduction

Micro-textured surfaces provide one of the oldest and most investigated methods of skin-friction drag reduction in wall-bounded turbulent flows (Bushnell & Hefner 1990). In earliest implementations, arrays of longitudinal microgrooves known as riblets, inspired by the microridges on the shark skin, were embedded in the walls to obtain drag reduction (Walsh 1980, 1982). Drag reductions of up to 10 % were achieved in laboratory-scale experiments with blade riblets of groove width $g^{+0} \equiv gu_{\tau_0}/\nu \approx 17$, groove depth $d/g \approx 0.5$, and groove spacing $w/g \approx 0.02$ (Bechert *et al.* 1997), where g, d and w denote the groove width, depth and spacing, respectively, as shown in figure 1(*a*), and the $+0$ superscript denotes normalization with respect to the kinematic viscosity, ν, and the wall friction velocity, u_{τ_0}, of a 'base' turbulent flow with smooth, no-slip walls, at the same bulk Reynolds number as the drag-reduced flow. In full-size applications, however, the drag reductions were more modest, of the order of 5–7 %, due to both the difficulties in employing thin blade riblets in practical applications (Bechert *et al.* 1997), and degradation of drag reduction performance of riblets with increasing Reynolds number, and decreasing friction coefficient, of the 'base' flow (Bechert *et al.* 1997; Spalart & McLean 2011).

More recently, superhydrophobic (SH) surfaces have received attention as a means of skin-friction drag reduction in turbulent flows (Rothstein 2010). These are surfaces with apparent receding contact angle exceeding a certain value, e.g. 150° (Schellenberger *et al.* 2016), in which nano- or micro-structured protrusions on a non-wetting solid surface entrap air underneath the liquid, leading to the so-called Cassie–Baxter state. The entrapped air prevents direct contact between the liquid and the wall, thus providing a mechanism for liquid slip at the walls. Drag reductions of up to 50 % and up to 75 % have been reported in laboratory-scale experiments in turbulent channel flows (Rothstein 2010) and turbulent boundary layer flows (Park, Sun & Kim 2014), with SH longitudinal microgrooves of size $2 \lesssim g^{+0} \lesssim 4$, $g/w = 1$ and $0.8 \lesssim g^{+0} \lesssim 1.6$, $g/w = 19$, respectively. Despite these remarkable results in laboratory-scale experiments, SH drag reduction has not yet evolved into a practical means of turbulent skin-friction control, mainly because under the high pressure and high shear rate conditions of turbulent flows in practical environments, the air pockets in the surface micro-texture either collapse (Checco *et al.* 2014) or dissolve into the working liquid (Karatay, Tsai & Lammertink 2013*a*). This has led to the development of more advanced, hierarchical, micro/nano textured surfaces (Feng *et al.* 2002; Wang *et al.* 2007; Kwon *et al.* 2009; Lee & Kim 2009; Cha *et al.* 2010; Lee & Kim 2011) and liquid infused surfaces (Wong *et al.* 2011; Rosenberg *et al.* 2016), to enhance the durability and robustness of SH surfaces.

Successful employment of micro-textured surfaces for drag reduction in turbulent flows of practical interest requires an in depth understanding of the mechanism and scaling of drag reduction with micro-textured surfaces, and the pressure and stress loads on the micro-textured surface. This understanding is only beginning to emerge from recent experimental, analytical and computational studies.

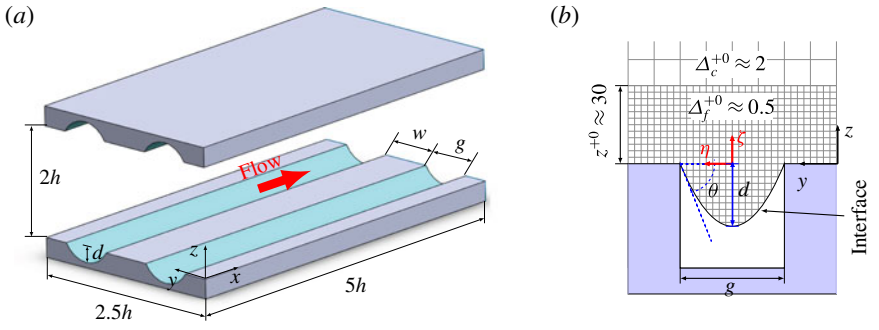

FIGURE 1. (*a*) Schematic of the channel and the coordinate system; (*b*) detailed view of the microgroove and the computational grid.

With riblets, it was recognized since the early days that their drag reduction characteristics can be described in terms of the difference, $\Delta h = h_{pl} - h_{pc}$, between two so-called 'protrusion heights', h_{pl} and h_{pc}, in the longitudinal and cross-flow directions, respectively (Bechert & Bartenwerfer 1989; Luchini, Manzo & Pozzi 1991; Bechert *et al.* 1997). These 'protrusion heights', which were defined as the distance between the rib tips and the average origin of the velocity profile near the surface, are none other than the 'slip lengths' in the streamwise and spanwise directions, defined as $L_{s,i} \equiv U_{s,i}/\langle \partial \overline{U}_i/\partial n \rangle|_{wall}$, where $U_{s,i}$ is the average slip velocity in the ith direction, n is the coordinate normal to the wall, and $\langle\ \rangle$ denotes averaging over the pattern of the surface micro-texture. Early studies, however, did not consider that the presence of such a 'slip length' in the streamwise direction implies the presence of a streamwise slip velocity, which can directly lead to drag reduction. Instead, they focused on the effect of the protrusion heights, h_{pl} and h_{pc}, on the dynamics of near-wall turbulence structures (Bechert & Bartenwerfer 1989; Luchini *et al.* 1991; Bechert *et al.* 1997). Two drag reduction regimes were identified: the 'viscous regime', operative at $g^{+0} \lesssim 10$–15, for which drag reduction increases almost linearly with increasing groove width; and the 'breakdown regime', operative at $g^{+0} \gtrsim 15$–20, for which viscous theory breaks down, and drag reduction saturates and begins to diminish with further increases in the groove width, eventually leading to net drag enhancement (Bechert *et al.* 1997). The optimal drag reduction performance was obtained with thin blade riblets of groove width $g^{+0} \approx 17$, for which $\Delta h = h_{pl} - h_{pc}$ was maximized (Bechert *et al.* 1997). More recently, it has been suggested that a better collapse of the drag reduction data in the 'viscous regime' can be obtained by parameterizing the magnitude of drag reduction in terms of the square root of the groove cross-sectional area, $l_g^+ \equiv \{A_g^+\}^{1/2}$, and that the optimal drag reduction performance is achieved at $l_g^+ \approx 10.7$ (Garcia-Mayoral & Jimenez 2011*a*), where the $+$ superscript denotes normalization with respect to the kinematic viscosity, ν, and the wall friction velocity, u_τ, in the flow with micro-textured walls. The drag reduction in the 'viscous regime' was attributed to the riblets hampering the cross-flow fluctuating velocity close to the wall, thus providing a resistance to the motion of near-wall streamwise vortical structures (Bechert & Bartenwerfer 1989; Walsh 1990; Luchini *et al.* 1991; Choi, Moin & Kim 1993; Chu & Karniadakis 1993; Goldstein, Handler & Sirovich 1995; Bechert *et al.* 1997). Deterioration of drag reduction in the 'breakdown regime' was attributed either to generation of secondary streamwise vorticity over the riblets, due to separation of the cross-flow (Goldstein & Tuan 1998), or to

appearance of large-scale spanwise rollers, which develop from a two-dimensional Kelvin–Helmholtz-like instability of the mean streamwise velocity, due to relaxation of the impermeability condition at the wall (Garcia-Mayoral & Jimenez 2011*a*). It was not until recently that it was recognized that the presence of a streamwise slip at the plane of riblet tips could by itself lead to drag reduction through augmenting the velocity of the free stream (Garcia-Mayoral & Jimenez 2011*a*,*b*).

With SH surfaces, the earliest direct numerical simulation (DNS) studies investigated the effect of a uniform streamwise or spanwise slip on turbulent skin-friction drag reduction in channel flow. It was shown that uniform streamwise slip leads to drag reduction by augmenting the bulk velocity, while uniform spanwise slip leads to drag enhancement by strengthening the near-wall streamwise vortical structures (Min & Kim 2004; Fukagata, Kasagi & Koumoutsakos 2006). Subsequent DNS studies considered the effect of various micro-patterns of surface slip, such as longitudinal or lateral stripes or tiles, as idealizations of the liquid/gas interfaces in real SH microgrooves or microposts with flat, shear-free boundaries (Martel, Perot & Rothstein 2009; Martel, Rothstein & Perot 2010; Rastegari & Akhavan 2013; Park, Park & Kim 2013; Jelly, Jung & Zaki 2014; Türk *et al.* 2014; Rastegari & Akhavan 2015; Seo, Garcia-Mayoral & Mani 2015; Jung, Choi & Kim 2016; Seo & Mani 2016). Surface slip was shown to be the dominant mechanism of turbulent skin-friction drag reduction with all of these surface micro-patterns, contributing between 80 to 100 % of the overall drag reduction (Rastegari & Akhavan 2015). Modifications to the turbulence structure and dynamics were shown to contribute no more than 20 % of the total drag reduction with longitudinal microgrooves or microposts of high shear-free fraction, and a drag increase with lateral microgrooves or microposts of moderate shear-free fraction (Rastegari & Akhavan 2015).

In all of these DNS studies, the liquid/gas interfaces on the SH surfaces were modelled as 'idealized', flat, shear-free boundaries. In reality, the liquid/gas interfaces on SH surfaces are not flat, but have a finite curvature (Ou & Rothstein 2005; Tsai *et al.* 2009; Rathgen & Mugel 2010). Experiments (Steinberger *et al.* 2007; Tsai *et al.* 2009; Karatay *et al.* 2013*b*), computations (Wang, Teo & Khoo 2014) and analytical studies (Sbragaglia & Prosperetti 2007; Crowdy 2016) in laminar flow have shown that this interface curvature can affect the slip length and drag reduction by negligible to significant amounts, depending on the size, geometry and orientation of the surface micro-texture relative to the flow, and whether the protrusion angle is positive or negative. In turbulent flow, however, no similar studies of the effect of interface curvature on SH drag reduction have yet been reported.

In this study, we report a first DNS investigation of the effect of interface curvature on turbulent skin-friction drag reduction with SH longitudinal microgrooves in channel flow. The liquid/gas interfaces in the SH microgrooves were modelled as stationary, curved, shear-free boundaries, with the shape of the meniscus determined from the solution of the Young–Laplace equation. This formulation does not allow the collapse or dissolving of the air pockets in the surface micro-texture. Thus the full range of negative protrusion angles, ranging from 0 to $-90°$, can be investigated. While negative protrusion angles beyond $-30°$, corresponding to contact angles greater than $120°$, cannot be sustained on smooth SH walls due to theoretical limits (Nishino *et al.* 1999), this limit can be bypassed by using hierarchical, micro/nano-scale SH surfaces (Feng *et al.* 2002; Wang *et al.* 2007; Kwon *et al.* 2009; Lee & Kim 2009; Cha *et al.* 2010; Lee & Kim 2011; Wong *et al.* 2011). In anticipation of deployment of such hierarchical SH surfaces in the future, the full range of negative protrusion angles has been investigated in the present study. For comparison, the same geometries as

those formed by the air/water interfaces in the SH longitudinal microgroove were also investigated as riblets, with the shear-free condition on the curved SH interfaces replaced with the no-slip boundary condition, to compare the mechanism of drag reduction in the two flows.

The paper is organized as follows. In § 2 the numerical methods and simulation parameters are reviewed. In § 3, an exact analytical expression for the magnitude of drag reduction in channel flows with any SH or no-slip micro-texture on the walls is derived. This expression allows the net drag reduction to be decomposed into its constitutive elements, thus clarifying the contribution of each element to the net drag reduction. In § 4, results from DNS in channel flows with micro-textured walls are used to evaluate the contribution of each of the terms in this analytical expression to the net drag reduction, to clarify the mechanism of drag reduction with SH longitudinal microgrooves and riblets. It will be shown that SH longitudinal microgrooves and riblets share a common mechanism of drag reduction. In § 5, extrapolation of these results to high Reynolds number flows of practical interest is discussed. In § 6, new possibilities for synergistic use of SH surfaces in conjunction with riblets is discussed, to reduce the pressure loads on SH surfaces and enhance their longevity and sustainability in turbulent flow environments. A summary and conclusions are presented in § 7.

2. Numerical methods and simulation parameters

The numerical simulations reported in this study were all performed using standard D3Q19 (3-Dimensional, 19 discrete velocity), single relaxation time lattice Boltzmann methods (Succi 2001) with grid embedding (Lagrava *et al.* 2012), of grid ratio 4:1, employed in the near-wall region, between the domain boundaries and the buffer layer ($z^{+0} \approx 30$), to improve the accuracy of the computations near the micro-textured walls. The resulting grid spacings were $\Delta_f^{+0} \approx 0.5$ for $z^{+0} \lesssim 30$, and $\Delta_c^{+0} \approx 2$ for $z^{+0} \gtrsim 30$, in all three directions, as shown in figure 1. In turbulent channel flows with smooth no-slip walls, the lattice Boltzmann method can fairly accurately predict the turbulent flow features with uniform grid spacings of $\Delta^{+0} \approx 2$ throughout the channel, as shown by Lammers *et al.* (2006) and discussed in appendix A, § A.2. With micro-textured surfaces, however, the presence of a slip velocity over the surface micro-indentations leads to steep wall-normal gradients of the streamwise velocity on the no-slip tips of the surface micro-texture, as well as strong shear layers between the slip and no-slip regions at the tip of the surface micro-texture. These shear layers persist up to distances of the order of $z \sim g$, but they become weaker with increasing distance from the wall, such that by $z^{+0} \gtrsim 30$ they can be properly resolved by the regular lattice Boltzmann grid of size $\Delta^{+0} \approx 2$, as shown in appendix A, § A.2. The grid-embedding scheme in the present study was employed to resolve these shear layers in the region $z^{+0} \lesssim 30$, as well as the steep wall-normal gradients of the velocity near the tips of the wall micro-texture.

The liquid/gas interfaces in the SH longitudinal microgrooves were modelled as stationary, curved, shear-free boundaries, with the shape of the meniscus determined from an analytical solution (de Gennes, Brochard-Wyart & Quéré 2002) of the Young–Laplace equation

$$\Delta\tilde{P} = -\frac{1}{We_{\tau_0}}\tilde{\nabla}\cdot\boldsymbol{n}, \tag{2.1}$$

where $\Delta\tilde{P} \equiv \Delta P/\rho u_{\tau_0}^2$ is the non-dimensional Laplace pressure across the interface, $We_{\tau_0} \equiv \rho u_{\tau_0}^2 g/\sigma$ is the Weber number, ρ is the fluid density, σ is the surface tension,

$\boldsymbol{n}$ is the unit normal to the interface and $\tilde{\boldsymbol{\nabla}}$ denotes the divergence operator in a non-dimensional local coordinate system, $(\tilde{\xi},\ \tilde{\eta},\ \tilde{\zeta}) = (\xi,\ \eta,\ \zeta)/g$, centred on the longitudinal microgroove, as shown in figure 1. Integrating (2.1), subject to the boundary conditions $\tilde{F}|_{(\tilde{\eta}=\pm 1/2)} = 0$ and $(\mathrm{d}\tilde{F}/\mathrm{d}\tilde{\eta})|_{(\tilde{\eta}=0)} = 0$, gives the shape of the interface as

$$\tilde{F}(\tilde{\eta}, \tilde{\kappa}) = -\frac{1}{2\tilde{\kappa}}\left(2\sqrt{1-\tilde{\kappa}^2\tilde{\eta}^2} - \sqrt{4-\tilde{\kappa}^2}\right), \tag{2.2}$$

where $\tilde{\kappa} = (\Delta\tilde{P}\cdot We_{\tau_0})$ is the non-dimensional curvature of the interface, which is related to the interface protrusion angle through

$$\theta = \tan^{-1}\left(\frac{\tilde{\kappa}}{2\sqrt{1-(\tilde{\kappa}/2)^2}}\right). \tag{2.3}$$

Equations (2.2) and (2.3) were used to determine the shape of the interface in the SH longitudinal microgrooves in the present study. Static protrusion angles of $\theta = 0°$, $-30°$, $-60°$ and $-90°$ were investigated, covering the full range of protrusion angles from flat interfaces to maximum negative protrusion angle. For comparison, the same geometries as those formed by the menisci of the SH longitudinal microgrooves were also simulated as riblets, with the free-slip boundary condition on the curved interfaces replaced with the no-slip boundary condition.

The boundary conditions on flat no-slip surfaces and flat free-slip interfaces were imposed using half-way bounce back and specular reflection methods (Succi 2001), respectively. The boundary conditions on the curved riblet walls were imposed using the so-called 'central linear interpolation' (CLI) scheme (Ginzburg, Verhaeghe & d'Humières 2008). This is a modified version of the half-way bounce back scheme, in which interpolations between pre- and post-collision distribution functions are used to find the unknown distributions at the boundaries while accounting for the full curvature of the wall. The boundary conditions on the curved SH interfaces were imposed using local specular reflection (Ginzburg & Steiner 2003). In this method, specular reflection is applied locally on the distribution functions in the vicinity of a stepwise realization of the curved interface, to reconstruct the unknown distributions at the boundaries. A number of verification studies were performed to ensure the accuracy of the numerical methods, the adequacy of the grid resolution, and the effect of domain size. These are described in appendix A.

All the simulations reported in the present study were performed in periodic channels of size $5h \times 2.5h \times 2h$ in the streamwise (x), spanwise (y), and wall-normal (z) directions, respectively, with SH longitudinal microgrooves or riblets on both walls, as shown in figure 1. For two cases, the simulations were repeated in channels of size $20h \times 10h \times 2h$, as discussed in appendix A, § A.3, to demonstrate the adequacy of the smaller domain size. A constant flow rate was maintained in the channels during the course of all the simulations, corresponding to bulk Reynolds numbers of $Re_b \equiv q/2\nu = 3600$ or $Re_b = 7860$, where q denotes the flow rate per unit spanwise width in the channel. A total of 12 simulations with SH longitudinal microgrooves and 9 simulations with riblets were performed at $Re_b = 3600$, corresponding to three longitudinal microgrooves of size $g^{+0} \approx 14$, 28, 56 and $g/w = 7$, each studied at four protrusion angles of $\theta = 0°$, $-30°$, $-60°$, $-90°$ as SH longitudinal microgrooves, and three protrusion angles of $\theta = -30°$, $-60°$, $-90°$ as riblets. In addition, the simulations with SH longitudinal microgrooves of size $g^{+0} \approx 14$, 28 and $g/w = 7$ at interface protrusion angle of $\theta = -30°$ were repeated at $Re_b = 7860$ to assess

the effect of the bulk Reynolds number on the drag reduction characteristics. For reference, DNS was also performed in 'base' turbulent channel flows with smooth, no-slip walls, at the same bulk Reynolds number as those in the channels with micro-textured walls. The cross-sectional area, A_0, in the 'base' turbulent channel flow was set to the 'nominal' cross-sectional area of the channel with micro-textured walls, as defined by area enclosed between the tips of the micro-textures on the opposing walls of the channel. The corresponding friction Reynolds numbers in the 'base' turbulent channel flows were $Re_{\tau_0} \equiv u_{\tau_0} h/\nu \approx 222$ at $Re_b = 3600$, and $Re_{\tau_0} \approx 442$ at $Re_b = 7860$. For comparison, all the above simulations were repeated in laminar flow at $Re_b = 150$. A summary of all the simulations performed in the present study is given in table 1.

3. Drag reduction with micro-textured surfaces in channel flow

Drag reduction with micro-textured surfaces involves contributions from a number of different dynamical effects, some of which are drag reducing, while others are drag enhancing. To clarify the mechanism of drag reduction, these effects need to be separated, so the contribution of each element can be assessed.

For turbulent channel, pipe and plane boundary layer flows with smooth no-slip walls, Fukagata, Iwamoto & Kasagi (2002) derived an analytical expression for the breakdown of the skin-friction coefficient into its constitutive elements. This derivation was later generalized to more geometrically complex no-slip surfaces by Peet & Sagaut (2009). In Rastegari & Akhavan (2015), the formulation of Fukagata *et al.* (2002) was used to derive an analytical expression for the breakdown of drag reduction into its constitutive elements for laminar or turbulent channel flows with any micro-pattern of 'flat' SH interfaces. In this section, the formulation of Rastegari & Akhavan (2015) will be generalized to channel flows with any three-dimensional SH or riblet micro-texture on the walls.

For steady, fully developed, turbulent channel flow with any SH or riblet micro-texture pattern on the walls, the streamwise Reynolds-averaged momentum equation is given by

$$\frac{\partial}{\partial x}\left(\nu\frac{\partial \bar{U}}{\partial x} - \overline{uu} - \bar{U}\bar{U}\right) + \frac{\partial}{\partial y}\left(\nu\frac{\partial \bar{U}}{\partial y} - \overline{uv} - \bar{U}\bar{V}\right) + \frac{\partial}{\partial z}\left(\nu\frac{\partial \bar{U}}{\partial z} - \overline{uw} - \bar{U}\bar{W}\right) = \frac{1}{\rho}\frac{\partial \bar{P}}{\partial x}, \tag{3.1}$$

where the overbar denotes Reynolds-averaging; $\bar{U}$, $\bar{V}$, $\bar{W}$ and u, v, w are the streamwise (x), spanwise (y) and wall-normal (z) components of the Reynolds-averaged mean and fluctuating velocities, respectively, and $\bar{P}$ is the Reynolds-averaged mean pressure. Equation (3.1) can also describe steady, laminar flow in a channel with any SH or riblet micro-texture pattern on the walls if u, v and w are set equal to zero.

Averaging (3.1) over the periodic pattern of the surface micro-texture in the streamwise and spanwise directions, and integrating in the wall-normal direction from the tip of the surface micro-texture, at $z = 0$, to a height z inside the channel (see figure 1), gives

$$\nu\left\langle\frac{\partial \bar{U}}{\partial z}\right\rangle - \langle\overline{uw}\rangle - \langle\bar{U}\bar{W}\rangle = -\frac{h}{\rho}\left\langle\frac{\partial \bar{P}}{\partial x}\right\rangle\left(1 - \frac{z}{h}\right), \tag{3.2}$$

where $\langle\ \rangle$ denotes averaging in the wall-parallel directions over the periodic pattern of the surface micro-texture; $2h$ is the 'nominal' full-height of the channel, defined as

https://doi.org/10.1017/jfm.2017.865 Published online by Cambridge University Press

$(g+w)/h$	0.072	0.072	0.072	0.072	0.144	0.144	0.144	0.144	0.288	0.288	0.288	0.288	0.036	0.072
g^{+0}	14	14	14	14	28	28	28	28	56	56	56	56	14	28
w^{+0}	2	2	2	2	4	4	4	4	8	8	8	8	2	4
θ	0°	−30°	−60°	−90°	0°	−30°	−60°	−90°	0°	−30°	−60°	−90°	−30°	−30°
A/A_0	1	1.005	1.011	1.022	1	1.010	1.023	1.043	1	1.020	1.045	1.087	1.003	1.005
SH longitudinal microgrooves														
Re_b (lam)	150	150	150	150	150	150	150	150	150	150	150	150	—	—
U_s/U_{b0}	0.131	0.127	0.126	0.125	0.205	0.196	0.192	0.190	0.325	0.308	0.301	0.296	—	—
DR (%)	13.1	11.5	9.8	7.1	20.5	17.4	14.2	9.1	32.5	27.4	22.1	13.6	—	—
DR_{slip} (%)	13.1	12.9	13.0	13.4	20.5	20.2	20.6	21.6	32.5	32.7	34.3	38.0	—	—
DR_{Q_g} (%)	—	−1.4	−3.2	−6.3	—	−2.8	−6.4	−12.5	—	−5.3	−12.2	−24.4	—	—
Re_b $(turb)$	3600	3600	3600	3600	3600	3600	3600	3600	3600	3600	3600	3600	7860	7860
U_s/U_{b0}	0.311	0.269	0.260	0.260	0.444	0.394	0.405	0.453	0.571	0.551	0.574	0.607	0.247	0.369
DR (%)	36.6	37.4	35.0	31.7	48.1	51.7	44.5	30.2	59.5	61.1	54.0	42.9	36.6	49.5
DR_{slip} (%)	31.1	27.3	26.9	27.7	44.3	40.6	43.3	51.4	57.1	58.5	65.6	77.9	24.9	37.4
DR_{ε} (%)	5.5	11.5	11.2	9.9	3.8	13.6	6.9	−10.3	2.4	7.3	−1.0	−14.8	12.4	13.4
$DR_{\langle\tau_R\rangle}$ (%)	5.6	11.9	11.3	10.3	5.6	17.6	8.3	−7.3	5.0	8.8	7.7	−3.1	12.5	14.0
$DR_{\langle\tau_R\rangle Re_{b_e}}$ (%)	18.8	16.2	14.1	19.4	25.2	21.7	24.9	41.0	35.1	30.0	44.8	69.4	15.1	21.6
$DR_{\langle\tau_R\rangle mod}$ (%)	−13.2	−4.3	−2.8	−9.1	−19.6	−4.1	−16.6	−48.3	−30.1	−21.2	−37.1	−72.5	−2.6	−7.6
$DR_{\langle\tau_c\rangle}$ (%)	−0.1	−0.4	−0.1	−0.4	−1.8	−4.0	−1.4	−3.0	−2.6	−1.5	−8.7	−11.7	−0.1	−0.6
DR_{Q_g} (%)	—	−1.4	−3.1	−5.9	—	−2.5	−5.7	−10.9	—	−4.7	−10.6	−20.2	−0.7	−1.3
$B-B_0$	4.71	4.87	4.44	3.89	7.12	8.02	6.28	3.64	10.40	10.96	8.67	5.94	5.12	8.10
U_s^+	6.33	5.54	5.30	5.22	9.99	9.29	9.01	9.18	14.55	14.62	14.36	14.15	5.53	9.27
l_g^+	—	3.32	5.06	7.11	—	5.81	9.25	14.07	—	10.32	16.47	24.44	3.35	5.96

TABLE 1. For caption see next page.

https://doi.org/10.1017/jfm.2017.865 Published online by Cambridge University Press

							Riblets							
Re_b (lam)	—	150	150	150	—	150	150	150	—	150	150	150	—	—
U_s/U_{b_0}	—	0.012	0.022	0.030	—	0.024	0.043	0.057	—	0.048	0.082	0.107	—	—
DR (%)	—	−0.3	−1.1	−3.4	—	−0.5	−2.3	−7.0	—	−1.0	−4.6	−14.0	—	—
DR_{slip} (%)	—	1.2	2.3	3.2	—	2.5	4.6	6.4	—	5.1	9.3	13.8	—	—
DR_{Q_g} (%)	—	−1.5	−3.4	−6.6	—	−3.0	−6.9	−13.4	—	−6.1	−13.9	−27.8	—	—
Re_b $(turb)$	—	3600	3600	3600	—	3600	3600	3600	—	3600	3600	3600	—	—
U_s/U_{b_0}	—	0.056	0.094	0.118	—	0.112	0.189	0.238	—	0.225	0.366	0.438	—	—
DR (%)	—	−0.3	2.7	5.0	—	0.0	−0.6	−3.4	—	−4.0	−13.2	−38.2	—	—
DR_{slip} (%)	—	5.7	9.7	12.6	—	11.5	20.2	27.0	—	23.9	41.8	56.2	—	—
DR_{ε} (%)	—	−4.5	−3.7	−1.1	—	−8.5	−14.1	−17.4	—	−22.0	−42.1	−69.5	—	—
$DR_{\langle\tau_R\rangle}$ (%)	—	−2.5	−2.3	0.2	—	−8.2	−11.6	−13.9	—	−17.5	−29.9	−38.8	—	—
$DR_{\langle\tau_R\rangle_{Re_{b_e}}}$ (%)	—	3.9	6.6	8.5	—	7.1	13.0	23.5	—	21.7	51.4	95.1	—	—
$DR_{\langle\tau_R\rangle_{mod}}$ (%)	—	−6.4	−8.9	−8.3	—	−15.3	−24.6	−37.4	—	−39.2	−81.3	−133.9	—	—
$DR_{\langle\tau_c\rangle}$ (%)	—	−2.0	−1.4	−1.3	—	−0.3	−2.5	−3.5	—	−4.5	−12.2	−30.7	—	—
DR_{Q_g} (%)	—	−1.5	−3.3	−6.5	—	−3.0	−6.7	−13.0	—	−5.9	−12.9	−24.9	—	—
$B - B_0$	—	−0.03	0.25	0.48	—	0.00	−0.05	−0.31	—	−0.36	−1.13	−2.83	—	—
U_s^+	—	0.92	1.57	2.00	—	1.83	3.12	3.96	—	3.65	5.84	6.56	—	—
l_g^+	—	4.21	6.19	8.38	—	8.36	12.44	17.13	—	16.88	25.83	38.03	—	—

TABLE 1 (cntd). Effective wall slip velocity, DR and its decomposition in laminar and turbulent channel flow with SH longitudinal microgrooves or riblets.

the distance between the tips of the surface micro-texture on the opposing walls of the channel; and we have used the identity $[\nu\langle\partial\bar{U}/\partial z\rangle - \langle\overline{uw}\rangle - \langle\bar{U}\bar{W}\rangle]_{z=0} = -\langle\partial\bar{P}/\partial x\rangle h/\rho$, as required by the force balance in the channel between $z=0$ and $z=2h$.

Integration of (3.2) in the wall-normal direction, once from 0 to z, and again from 0 to h (Fukagata *et al.* 2002; Rastegari & Akhavan 2015), gives

$$-\frac{h}{\rho U_{b_0}^2}\left\langle\frac{\partial\bar{P}}{\partial x}\right\rangle\left(1-3\int_0^1\left(\frac{-\langle\overline{uw}\rangle-\langle\bar{U}\bar{W}\rangle}{-\frac{h}{\rho}\left\langle\frac{\partial\bar{P}}{\partial x}\right\rangle}\right)(1-\chi)\,\mathrm{d}\chi\right)=\frac{3}{Re_b}\left(1-\frac{Q_g}{Q}-\frac{U_s}{U_{b_0}}\right). \tag{3.3}$$

Here, U_{b_0} is the bulk velocity in a smooth, no-slip 'base' channel flow with the same bulk Reynolds number, $Re_b \equiv q/2\nu$, hence the same flow rate per unit spanwise width, $q \equiv Q/L_y$, and the same bulk flow rate, Q, as the channel with micro-textured walls, and a 'base' channel flow cross-sectional area, A_0, equal to the 'nominal' cross-sectional area of the channel with micro-textured walls, as defined by the area enclosed between the tips of the surface micro-texture on the opposing walls of the channel; Q_g is the flow rate through the surface micro-texture indentations; $U_s \equiv \langle\bar{U}\rangle|_{z=0}$ is the average slip velocity at the tip of the surface micro-texture; and $\chi \equiv z/h$ is the non-dimensional wall-normal coordinate. Equation (3.3) can be rearranged as

$$-\frac{h}{\rho U_{b_0}^2}\left\langle\frac{\partial\bar{P}}{\partial x}\right\rangle=\frac{3}{Re_b}\left(1-\frac{Q_g}{Q}-\frac{U_s}{U_{b_0}}\right)\left(\frac{1}{1-3I}\right), \tag{3.4}$$

where $I = I_{\langle\tau_R\rangle} + I_{\langle\tau_c\rangle} = [1/(-\langle\partial\bar{P}/\partial x\rangle h/\rho)]\int_0^1(-\langle\overline{uw}\rangle - \langle\bar{U}\bar{W}\rangle)(1-\chi)\,\mathrm{d}\chi$ denotes the contribution of the turbulent Reynolds shear stresses, $\langle\tau_R\rangle \equiv -\rho\langle\overline{uw}\rangle$, and any mean flow shear stresses, $\langle\tau_c\rangle \equiv -\rho\langle\bar{U}\bar{W}\rangle$, established in the channel due to the presence of the micro-texture on the walls, to the overall wall shear stress, and I is bounded by $0 < I < 1/3$ per (3.2). For the 'base' channel flow with smooth no-slip walls, (3.4) reduces to

$$-\frac{h}{\rho U_{b_0}^2}\left\langle\frac{\partial\bar{P}}{\partial x}\right\rangle_0=\frac{3}{Re_b}\left(\frac{1}{1-3I_0}\right), \tag{3.5}$$

where $I_0 = I_{\langle\tau_R\rangle_0} = [1/(-\langle\partial\bar{P}/\partial x\rangle_0 h/\rho)]\int_0^1 -\langle\overline{uw}\rangle_0(1-\chi)\,\mathrm{d}\chi$.

Using the definition $DR \equiv (1 - C_f/C_{f_0})$, the magnitude of drag reduction can be expressed as

$$DR\equiv\left(1-\frac{C_f}{C_{f_0}}\right)=\left(1-\frac{\left(\frac{\tau_w}{\rho(Q/A)^2}\right)}{\left(\frac{\tau_{w_0}}{\rho(Q/A_0)^2}\right)}\right)=\left(1-\frac{\left\langle\frac{\partial\bar{P}}{\partial x}\right\rangle}{\left\langle\frac{\partial\bar{P}}{\partial x}\right\rangle_0}\left(\frac{A}{A_0}\right)^3\right), \tag{3.6}$$

where $C_f \equiv \tau_w/[\rho(Q/A)^2]$ and $C_{f_0} \equiv \tau_{w_0}/[\rho(Q/A_0)^2]$ are the skin-friction coefficients, τ_w and τ_{w_0} are the wall shear stresses, A and A_0 are the cross-sectional areas, and (Q/A) and (Q/A_0) are the bulk velocities, in the channel with micro-textured walls and the 'base' channel flow, respectively.

Substitution of (3.4) and (3.5) into (3.6) gives

$$\begin{aligned} DR &= \left\{\left(\frac{A}{A_0}\right)^3\left(\frac{U_s}{U_{b_0}}\right)\right\} + \left\{\left(\frac{A}{A_0}\right)^3\left(1-\frac{U_s}{U_{b_0}}-\frac{Q_g}{Q}\right)\left(\frac{3\varepsilon}{1-3I}\right)\right\} \\ &\quad + \left\{1-\left(\frac{A}{A_0}\right)^3\left(1-\frac{Q_g}{Q}\right)\right\} \\ &= \{DR_{slip}\} + \{DR_{\varepsilon}\} + \{DR_{Q_g}\}, \end{aligned} \tag{3.7}$$

where $\varepsilon = (I_0 - I)$ is a measure of the changes in the normalized structure of turbulent Reynolds shear stresses and any mean flow shear stresses developed in the channel due to the presence of the micro-texture on the walls, compared to a 'base' channel flow with smooth no-slip walls.

Equation (3.7) provides an exact analytical expression for the magnitude of drag reduction in laminar or turbulent channel flow with any SH or no-slip micro-texture on the walls, while providing a decomposition of drag reduction into: (i) the contributions arising from the effective slip velocity at the wall, represented by $\{DR_{slip}\}$; (ii) the contributions arising from modifications to the structure of turbulent Reynolds shear stresses and any mean flow shear stresses developed in the channel due to the presence of the wall micro-texture, represented by $\{DR_{\varepsilon}\}$; and (iii) the contributions arising from the fraction of the flow rate through the wall micro-texture, represented by $\{DR_{Q_g}\}$.

The term $\{DR_{\varepsilon}\}$ in (3.7) involves contributions from several different dynamical effects, and can be further decomposed. To begin with, one can decompose $\varepsilon = (I_0 - I) = (I_{\langle\tau_R\rangle_0} - I_{\langle\tau_R\rangle} - I_{\langle\tau_c\rangle})$ into

$$\varepsilon = \varepsilon_{\langle\tau_R\rangle} + \varepsilon_{\langle\tau_c\rangle}, \tag{3.8}$$

where $\varepsilon_{\langle\tau_R\rangle} = (I_{\langle\tau_R\rangle_0} - I_{\langle\tau_R\rangle})$ represents the contributions arising from changes in the normalized structure of turbulent Reynolds shear stresses, and $\varepsilon_{\langle\tau_c\rangle} = (-I_{\langle\tau_c\rangle})$ represents the contributions arising from changes in the structure of the mean flow shear stresses, due to the presence of the wall micro-texture. Furthermore, the contributions from $\varepsilon_{\langle\tau_R\rangle} = (I_{\langle\tau_R\rangle_0} - I_{\langle\tau_R\rangle})$ can themselves be decomposed into

$$\varepsilon_{\langle\tau_R\rangle} = \varepsilon_{\langle\tau_R\rangle_{Re_{b_e}}} + \varepsilon_{\langle\tau_R\rangle_{mod}}, \tag{3.9}$$

where $\varepsilon_{\langle\tau_R\rangle_{Re_{b_e}}} = (I_{\langle\tau_R\rangle_0} - I_{\langle\tau_R\rangle_{Re_{b_e}}})$ and $\varepsilon_{\langle\tau_R\rangle_{mod}} = (I_{\langle\tau_R\rangle_{Re_{b_e}}} - I_{\langle\tau_R\rangle})$, and $I_{\langle\tau_R\rangle_{Re_{b_e}}}$ is the value of the I integral in a channel flow with smooth no-slip walls at bulk Reynolds number equal to $Re_{b_e} = (1 - U_s/U_b)Re_b$. The decomposition (3.9) is made in consideration of the fact that the presence of an effective slip velocity, U_s, implies that a fraction, U_s/U_b, of the flow rate can flow inviscidly (Min & Kim 2004; Fukagata *et al.* 2006). This reduces the effective bulk Reynolds number of the viscous part of the flow from Re_b to $Re_{b_e} = (1 - U_s/U_b)Re_b$. As such, $\varepsilon_{\langle\tau_R\rangle_{Re_{b_e}}}$ represents the changes to the normalized structure of turbulent Reynolds shear stresses in a channel flow with smooth no-slip walls when the bulk velocity, U_b, is augmented by the presence of an effective wall slip velocity, U_s, in effect reducing the bulk Reynolds number of the viscous part of the flow from Re_b to Re_{b_e}, while $\varepsilon_{\langle\tau_R\rangle_{mod}}$ represents the contributions from any other modifications to the normalized structure of the turbulent Reynolds shear stresses due to the presence of the micro-texture on the walls.

The integral $I_{\langle\tau_R\rangle_{Re_{b_e}}} = [1/(-\langle\partial\bar{P}/\partial x\rangle_{Re_{b_e}} h/\rho)] \int_0^1 -\langle\overline{uw}\rangle_{Re_{b_e}}(1-\chi)\,\mathrm{d}\chi$, required for the evaluation of $\varepsilon_{\langle\tau_R\rangle_{Re_{b_e}}}$ and $\varepsilon_{\langle\tau_R\rangle_{mod}}$, can be computed directly from its definition, by

performing additional DNS in smooth no-slip channel flows at bulk Reynolds number equal to Re_{b_e}. Alternatively, $I_{\langle\tau_R\rangle Re_{b_e}}$ can be computed by using the relation $I_{\langle\tau_R\rangle Re_{b_e}} = (1/3)[1-(3/Re_{b_e})(U_{b_e}/u_{\tau_e})^2]$, which can be obtained from (3.5) for any smooth-wall no-slip turbulent channel flow, where U_{b_e} and u_{τ_e} represent the bulk velocity and the wall friction velocity, respectively, in a turbulent channel flow at a bulk Reynolds number of Re_{b_e}. The ratio (U_{b_e}/u_{τ_e}) can be evaluated from DNS, or from experimental correlations such as Dean's correlation (Dean 1978). In the present study, the integrals $I_{\langle\tau_R\rangle Re_{b_e}}$ were evaluated by performing additional DNS at bulk Reynolds number equal to Re_{b_e}.

With these additional decompositions of $\{DR_\varepsilon\}$, (3.7) can be written as

$$\begin{aligned} DR &= \left\{\left(\frac{A}{A_0}\right)^3\left(\frac{U_s}{U_{b_0}}\right)\right\} \\ &\quad + \left\{\left(\frac{A}{A_0}\right)^3\left(1-\frac{U_s}{U_{b_0}}-\frac{Q_g}{Q}\right)\left(\frac{3\{\varepsilon_{\langle\tau_R\rangle Re_{b_e}}+\varepsilon_{\langle\tau_R\rangle mod}+\varepsilon_{\langle\tau_c\rangle}\}}{1-3I}\right)\right\} \\ &\quad + \left\{1-\left(\frac{A}{A_0}\right)^3\left(1-\frac{Q_g}{Q}\right)\right\} \\ &= \{DR_{slip}\}+\{DR_{\langle\tau_R\rangle}+DR_{\langle\tau_c\rangle}\}+\{DR_{Q_g}\} \\ &= \{DR_{slip}\}+\{DR_{\langle\tau_R\rangle Re_{b_e}}+DR_{\langle\tau_R\rangle mod}+DR_{\langle\tau_c\rangle}\}+\{DR_{Q_g}\}. \end{aligned} \tag{3.10}$$

Equation (3.10) shows that the net drag reduction in laminar or turbulent channel flow with any SH or riblet micro-texture pattern on the walls can be decomposed into (i) contributions arising from the effective slip velocity at the wall, represented by $\{DR_{slip}\}$; (ii) contributions arising from modifications to the normalized structure of turbulent Reynolds shear stresses due to augmentation of the bulk velocity by the effective slip velocity at the wall, represented by $\{DR_{\langle\tau_R\rangle Re_{b_e}}\}$; (iii) contributions arising from other modifications to the normalized structure of turbulent Reynolds shear stresses due to the presence of the micro-texture on the walls, represented by $\{DR_{\langle\tau_R\rangle mod}\}$; (iv) contributions arising from any mean flow shear stresses developed due to presence of the micro-texture on the walls, represented by $\{DR_{\langle\tau_c\rangle}\}$; and (v) contributions arising from the fraction of the flow rate through the wall micro-texture, represented by $\{DR_{Q_g}\}$.

For SH channel flows with 'idealized' flat liquid/gas interfaces, $(A/A_0)=1$ and $Q_g=0$, and (3.7) or (3.10) reduce to the expression (2.5) given in Rastegari & Akhavan (2015). Each of the terms in (3.7) or (3.10) can be evaluated using results from DNS to clarify the mechanism of drag reduction with micro-textured surfaces.

4. Results

4.1. *The mechanism of drag reduction with SH longitudinal microgrooves and riblets*

Table 1 and figures 2 and 3 show the wall slip velocities, the magnitudes of DR and the decomposition of DR into its constitutive elements obtained from DNS of laminar and turbulent channel flows with SH longitudinal microgrooves or riblets in the present study.

In laminar flow, (3.7) or (3.10) reduce to $DR = \{DR_{slip}\} + \{DR_{Q_g}\}$, where $\{DR_{slip}\} = \{(A/A_0)^3(U_s/U_{b_0})\}$ and $\{DR_{Q_g}\} = \{1-(A/A_0)^3(1-Q_g/Q)\}$. The wall

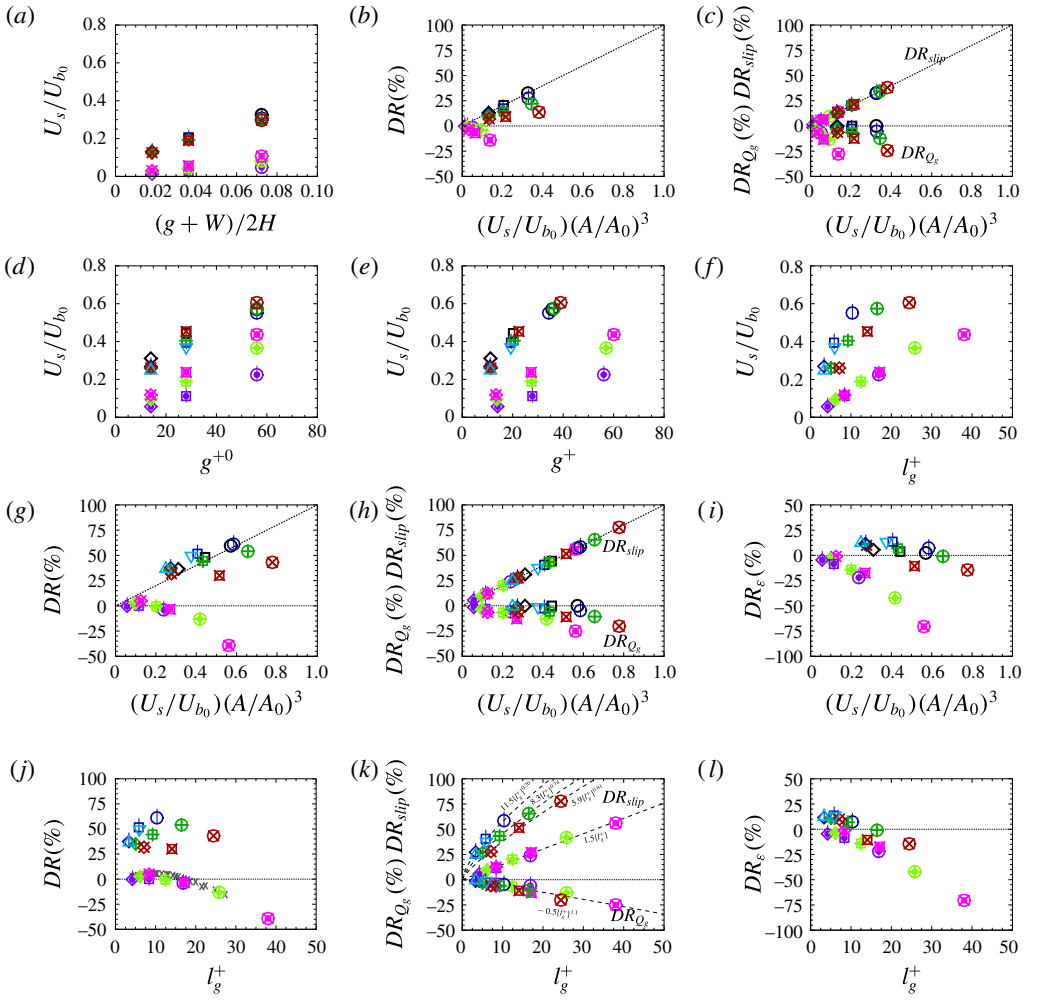

FIGURE 2. Effective wall slip velocity, DR and its decomposition into its constitutive elements in (*a–c*) laminar, and (*d–l*) turbulent channel flow with SH longitudinal Micro-Grooves (LMGs) or riblets: (*a*,*d*,*e*,*f*) effective wall slip velocity; (*b*,*g*,*j*) DR; (*c*,*h*,*i*,*k*,*l*) decomposition of DR. ◇, □, ○ (black), SH LMGs, $Re_b = 3600$, $\theta = 0°$, $g^{+0} \approx 14$, 28, 56; ◈, ⊞, ⊕ (dark blue), SH LMGs, $Re_b = 3600$, $\theta = -30°$, $g^{+0} \approx 14$, 28, 56; ◈, ⊞, ⊕ (dark green), SH LMGs, $Re_b = 3600$, $\theta = -60°$, $g^{+0} \approx 14$, 28, 56; ◈, ⊠, ⊗ (dark red), SH LMGs, $Re_b = 3600$, $\theta = -90°$, $g^{+0} \approx 14$, 28, 56; △, ▽ (light blue), SH LMGs, $Re_b = 7860$, $\theta = -30°$, $g^{+0} \approx 14$, 28; ◈, ⊞, ⊕ (violet) riblets, $Re_b = 3600$, $\theta = -30°$, $g^{+0} \approx 14$, 28, 56; ◈, ⊞, ⊕ (apple green), riblets, $Re_b = 3600$, $\theta = -60°$, $g^{+0} \approx 14$, 28, 56; ◈, ⊠, ⊗ (magenta), riblets, $Re_b = 3600$, $\theta = -90°$, $g^{+0} \approx 14$, 28, 56; × (grey), experimental data of Bechert *et al.* (1997) at $5000 \leqslant Re_b \leqslant 16\,500$ with semi-circular scalloped riblets; ·····, $DR = (U_s/U_{b_0})(A/A_0)^3$.

slip velocity, (U_s/U_{b_0}), increases with increasing microgroove width for both SH longitudinal microgrooves and riblets, as shown in figure 2(*a*) and table 1. However, the slip velocities obtained with SH longitudinal microgrooves are ∼3–10 times larger than those obtained with riblets, depending on the microgroove width and

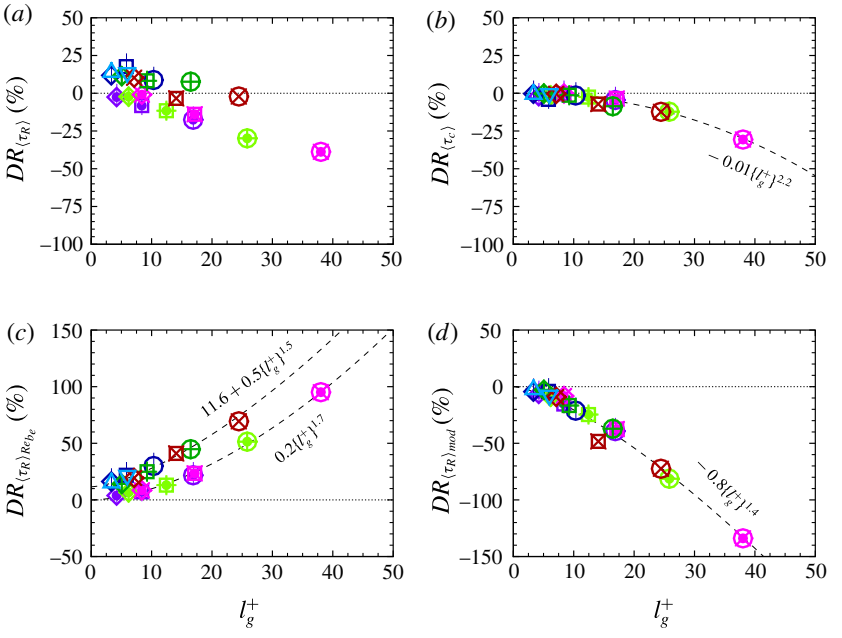

FIGURE 3. Decomposition of DR_ε into its constitutive elements: (*a*) $DR_{\langle\tau_R\rangle}$; (*b*) $DR_{\langle\tau_c\rangle}$; (*c*) $DR_{\langle\tau_R\rangle Re_{b_e}}$; (*d*) $DR_{\langle\tau_R\rangle mod}$. Symbols as in figure 2.

depth. The interface protrusion angle has a relatively minor effect on the magnitude of the slip velocity with SH longitudinal microgrooves, leading to drops of no more than 5–10 % in (U_s/U_{b_0}) with increasing protrusion angle, compared to flat interfaces. With riblets, however, the wall slip velocity increases by factors of ∼2.2–2.5 as the riblet microgroove depth increases from $d/g \approx 0.13$, at $\theta = -30°$, to $d/g = 0.5$, at $\theta = -90°$. Both the drop in SH longitudinal microgroove slip velocity with protrusion angle and the increase in riblet slip velocity with microgroove depth reflect the displacement of the slip or no-slip boundaries away from the microgroove tips with increasing protrusion angle or microgroove depth.

The presence of an effective wall slip velocity, U_s, implies that a fraction $(U_s/U_b) = (A/A_0)(U_s/U_{b_0})$ of the bulk velocity can flow inviscidly, leading to drag reduction through the $\{DR_{slip}\}$ term in (3.7) or (3.10). However, a part of this drag reduction is negated by $\{DR_{Q_g}\}$, which is always drag enhancing, as shown in figure 2(*c*) and table 1. In laminar flow with SH longitudinal microgrooves, the drag enhancing contributions from $\{DR_{Q_g}\}$ lead only to deviations of the net drag reduction from the line $DR = \{DR_{slip}\}$, while with riblets, the drag enhancing contributions from $\{DR_{Q_g}\}$ completely negate the drag reduction due to $\{DR_{slip}\}$ and lead to negative net drag reductions, as shown in figure 2(*b*) and table 1. This is the case even though the magnitudes of $\{DR_{Q_g}\}$ in laminar flow with riblets are comparable to, and only slightly higher than, those with SH longitudinal microgrooves for a given geometry of the wall micro-texture.

Similar features can also be observed for $\{DR_{slip}\}$ and $\{DR_{Q_g}\}$ in turbulent flow, as shown in figure 2(*d*,*h*) and table 1. For a given geometry of the surface micro-texture, the magnitudes of $\{DR_{Q_g}\}$ for SH longitudinal microgrooves and riblets remain comparable to each other and to their respective values in laminar flow, as shown

in figure 2(*h*). However, the normalized slip velocities, (U_s/U_{b_0}), in turbulent flow are significantly larger than those in laminar flow, by factors of ∼2 for SH longitudinal microgrooves, and by factors of ∼4–5 for riblets, respectively. The interface protrusion angle has a relatively minor effect on the slip velocity with SH longitudinal microgrooves in turbulent flow, as well, leading to drops of no more than 16 % or increases of no more than 6 % in (U_s/U_{b_0}) compared to flat interfaces, depending on whether the maximum interface depth is $d^+ \lesssim 10$ or $d^+ \gtrsim 10$. In the former, the slip velocity decreases with increasing interface depth, similar to laminar flow, while in the latter, the trends are reversed, and the slip velocity is enhanced with increasing interface depth. With riblets, the slip velocity increases by factors of ∼2, for all microgroove widths, as the riblet microgroove depth increases from $d/g \approx 0.13$, at $\theta = -30°$, to $d/g = 0.5$ at, $\theta = -90°$, similar to laminar flow.

Figure 2(*e*,*f*) shows the normalized slip velocities in turbulent flow plotted as a function of the microgroove width, g^+, and as a function of the square root of the microgroove cross-sectional area, $l_g^+ = \{A_g^+\}^{1/2}$ (Garcia-Mayoral & Jimenez 2011*a*), respectively. The best collapse of the data is observed when the data are plotted as a function of l_g^+, as shown in figure 2(*f*), in agreement with the observations of Garcia-Mayoral & Jimenez (2011*a*).

Figure 2(*k*) shows $\{DR_{slip}\}$ and $\{DR_{Q_g}\}$ in turbulent flow plotted as a function of l_g^+. The trends in the data begin to emerge when they are plotted in this manner as a function of l_g^+. The $\{DR_{Q_g}\}$ data for both SH longitudinal microgrooves and riblets nearly collapse and follow the scaling $\{DR_{Q_g}\} \sim -0.5\{l_g^+\}^{1.1}$. The $\{DR_{slip}\}$ data for riblets collapse to the line $\{DR_{slip}\} \sim 1.5\{l_g^+\}$, while the $\{DR_{slip}\}$ data for SH longitudinal microgrooves follow scalings which range from $\{DR_{slip}\} \sim 11.5\{l_g^+\}^{0.7}$ at $\theta = -30°$, to $\{DR_{slip}\} \sim 5.9\{l_g^+\}^{0.81}$ at $\theta = -90°$, indicating that with increasing microgroove depth, the scaling of $\{DR_{slip}\}$ with SH longitudinal microgrooves begins to approach that of riblets.

In turbulent flow, however, beyond the contributions from $\{DR_{slip}\}$ and $\{DR_{Q_g}\}$, there is also an additional contribution to drag reduction from $\{DR_\varepsilon\}$, representing the drag reduction or drag increase arising from changes to the structure of turbulent Reynolds shear stresses and any mean flow shear stresses which develop due to the presence of the wall micro-texture, as shown by (3.7) and figure 2(*i*,*l*). When plotted as a function of l_g^+, SH longitudinal microgrooves and riblets show nearly parallel trends in $\{DR_\varepsilon\}$, with the $\{DR_\varepsilon\}$ data for SH longitudinal microgrooves shifted relative to the data for riblets, as shown in figure 2(*l*). With SH longitudinal microgrooves, $\{DR_\varepsilon\}$ is drag reducing for microgrooves of characteristic size $l_g^+ \lesssim 10.5$, and drag enhancing for microgrooves of characteristic size $l_g^+ \gtrsim 10.5$, contributing up to ∼14 % additional drag reduction or up to ∼15% drag increase, respectively. With riblets, $\{DR_\varepsilon\}$ is always drag enhancing, but becomes strongly drag enhancing for riblets of characteristic size $l_g^+ \gtrsim 10.5$.

With SH longitudinal microgrooves, these contributions from $\{DR_{Q_g}\}$ and $\{DR_\varepsilon\}$ lead only to deviations of the net drag reduction from the line $DR = \{DR_{slip}\}$, as shown in figure 2(*g*). For a given width of the SH longitudinal microgrooves in base flow wall units, the highest and lowest drag reductions were always obtained at $\theta = -30°$ and $\theta = -90°$, as shown in figure 2(*g*, *j*), resulting in drag reductions which differ from those with flat SH interfaces by up to +3.6 % to −18 %, respectively. The highest drag reductions, of ≈61 %, were obtained with SH microgrooves of size $g^{+0} \approx 56$, $w^{+0} \approx 8$ at the protrusion angle of $\theta = -30°$. With riblets, the net drag reduction follows the line $DR = \{DR_{slip}\}$ only for microgrooves of characteristic size $l_g^+ \lesssim 10.5$, as shown in

figure 2(*g*,*j*). For $l_g^+ \gtrsim 10.5$, the drag enhancing contributions from $\{DR_\varepsilon\}$ and $\{DR_{Q_g}\}$ cause a decline in the magnitude of drag reduction, eventually leading to a net drag increase for $l_g^+ \gtrsim 17$. The highest magnitude of drag reduction obtained with riblets in the present study was 5 %, obtained for riblets of size $g^{+0} \approx 14$, $w^{+0} \approx 2$ at $\theta = -90°$ ($l_g^+ \sim 8.5$). The magnitudes of drag reduction observed with riblets in the present study are consistent with experimental measurements reported by Bechert *et al.* (1997) for semi-circular scalloped riblets with $d/g = 0.5$, as shown in figure 2(*j*).

To gain a better understanding of the source of the differences between $\{DR_\varepsilon\}$ with SH longitudinal microgrooves and riblets, one can decompose $\{DR_\varepsilon\}$ into its constitutive elements, as discussed in § 3 and shown in figure 3. To begin with, the contributions from $\{DR_\varepsilon\}$ can be decomposed into $\{DR_\varepsilon\} = \{DR_{\langle\tau_R\rangle}\} + \{DR_{\langle\tau_c\rangle}\}$, as shown by (3.10), where $\{DR_{\langle\tau_R\rangle}\}$ and $\{DR_{\langle\tau_c\rangle}\}$ represent the contributions to drag reduction arising from modifications to the normalized structure of turbulent Reynolds shear stresses and any mean flow shear stresses which develop due to the presence of the wall micro-texture, respectively. DNS results, displayed in figure 3(*a*,*b*), show that $\{DR_{\langle\tau_R\rangle}\}$ is drag reducing for SH longitudinal microgrooves of depth $d^+ \lesssim 10.5$, but drag enhancing with riblets of any size and SH longitudinal microgrooves of depth $d^+ \gtrsim 10.5$, while $\{DR_{\langle\tau_c\rangle}\}$ is always drag enhancing and follows a common scaling with both SH longitudinal microgrooves and riblets when plotted as a function of l_g^+. The finding that $DR_{\langle\tau_R\rangle}$ is always drag enhancing with riblets stands in contrast with current understanding of the mechanism of drag reduction with riblets, which attributes at least part of the drag reduction with riblets to the weakening of turbulent vortical structures (Bechert & Bartenwerfer 1989; Walsh 1990; Luchini *et al.* 1991; Chu & Karniadakis 1993; Goldstein *et al.* 1995; Bechert *et al.* 1997; Garcia-Mayoral & Jimenez 2011*a*).

The differences between $\{DR_{\langle\tau_R\rangle}\}$ with SH longitudinal microgrooves and riblets can be further understood by decomposing $\{DR_{\langle\tau_R\rangle}\}$ into $\{DR_{\langle\tau_R\rangle}\} = \{DR_{\langle\tau_R\rangle Re_{b_e}}\} + \{DR_{\langle\tau_R\rangle_{mod}}\}$, as shown in (3.10) and figure 3(*c*,*d*), where $\{DR_{\langle\tau_R\rangle Re_{b_e}}\}$ represents the contributions to drag reduction arising from changes to the normalized structure of turbulent Reynolds shear stresses due to the presence of an effective slip velocity, U_s, at the wall, which in effect reduces the bulk Reynolds number of the viscous part of the flow from Re_b to $Re_{b_e} = (1 - U_s/U_b)Re_b$, while $\{DR_{\langle\tau_R\rangle_{mod}}\}$ represents the contributions to drag reduction arising from any other modifications to the normalized structure of turbulent Reynolds shear stresses in the presence of the surface micro-texture. By definition, the contributions from $\{DR_{\langle\tau_R\rangle Re_{b_e}}\}$ are always drag reducing. Figure 3(*c*,*d*) shows that these contributions follow nearly parallel trends with SH longitudinal microgrooves and riblets, while the contributions from $\{DR_{\langle\tau_R\rangle_{mod}}\}$ are always drag enhancing and follow a common scaling with SH longitudinal microgrooves and riblets when plotted as a function of l_g^+.

The results displayed in figures 2 and 3 quantify and clarify the contribution of each of the five terms in (3.10) to the net drag reduction with SH longitudinal microgrooves or riblets in laminar or turbulent flow. These five contributions are: (i) the effective slip velocity at the wall, which allows a fraction (U_s/U_b) of the flow rate to be carried inviscidly, represented by $\{DR_{slip}\}$; (ii) modifications to the normalized structure of turbulent Reynolds shear stresses due to the drop in the bulk Reynolds number of the 'viscous' part of the flow, from Re_b to $Re_{b_e} = (1 - U_s/U_b)Re_b$, because of the presence of this effective slip velocity at the wall, represented by $\{DR_{\langle\tau_R\rangle Re_{b_e}}\}$; (iii) other modifications to the normalized structure of turbulent Reynolds shear stresses due to the presence of the surface micro-texture, represented by $\{DR_{\langle\tau_R\rangle_{mod}}\}$; (iv) mean

flow shear stresses developed due to presence of the surface micro-texture, represented by $\{DR_{\langle\tau_c\rangle}\}$; and (v) the fraction of the flow rate through the surface micro-texture, represented by $\{DR_{Q_g}\}$.

DNS results with SH longitudinal microgrooves and riblets, displayed in figures 2(*c*,*k*) and 3(*b*–*d*), show that SH longitudinal microgrooves and riblets share a common mechanism of drag reduction, in which 100 % of the drag reduction arises from effects (i) and (ii). The contributions from (iii)–(v) were always drag enhancing, and followed common scalings with SH longitudinal microgrooves and riblets when expressed as a function of l_g^+. These results indicate that the differences in the drag reduction performance of SH longitudinal microgrooves and riblets can be attributed entirely to the different magnitudes of the effective slip velocity which can be achieved in the two flows.

4.2. *Turbulence statistics*

The common mechanism of drag reduction with SH longitudinal microgrooves and riblets also leads to common features in the normalized profiles of the spanwise-averaged mean streamwise velocities, $\langle\overline{U}\rangle^+$, turbulence intensities, $\{\langle\overline{u_i^2}\rangle^{1/2}\}^+$, Reynolds shear stresses, $\langle\tau_{R,xz}\rangle^+$, and mean convective shear stresses, $\langle\tau_{c,xz}\rangle^+$, in the two flows, as shown in figure 4. With the effective wall slip velocity subtracted, the mean streamwise velocity profiles, $\langle\overline{U}\rangle^+ - U_s^+$, with both SH longitudinal microgrooves and riblets display a shortening of the viscous sublayer and the buffer layer, and a downward shift of the logarithmic layer, with comparable magnitudes of the shift for SH longitudinal microgrooves and riblets of comparable characteristic size, l_g^+, as shown in figures 4(*a*,*d*), 4(*g*,*j*) and 4(*m*,*p*). These features provide further confirmation of the findings in § 4.1 that, beyond the effect of U_s, the presence of the wall micro-texture leads only to drag enhancement through the $\{DR_{\langle\tau_R\rangle_{mod}}\}$ and $\{DR_{\langle\tau_c\rangle}\}$ terms, and that these two terms have similar effects on the structure and dynamics of turbulence with SH longitudinal microgrooves and riblets of a given characteristic size, l_g^+.

The normalized profiles of turbulence intensities with both SH longitudinal microgrooves and riblets show enhanced magnitudes of turbulence intensities, compared to the base flow, within a 'surface layer' of thickness $\sim 2g$, for all components of turbulent velocity fluctuations, as shown in figures 4(*b*,*e*), 4(*h*,*k*) and 4(*n*,*q*). These enhanced turbulence intensities result from additional production of streamwise turbulence kinetic energy, due to presence of spanwise gradients of the Reynolds-averaged streamwise velocity, $\partial\overline{U}/\partial y$, between the slip and no-slip regions at the tip of the surface micro-texture, which are then transferred to the wall-normal and cross-stream components of the turbulent velocity fluctuations through the pressure-strain terms.

The changes to the structure of turbulence and the mean flow affect the drag reduction only through the changes in the Reynolds shear stresses, $\langle\tau_{R,xz}\rangle$, and mean convective shear stresses, $\langle\tau_{c,xz}\rangle$, compared to the base flow, as shown by the $\{DR_{\langle\tau_R\rangle}\}$ and $\{DR_{\langle\tau_c\rangle}\}$ terms in (3.10). These shear stresses are displayed in figure 4(*c*,*f*,*i*,*l*,*o*,*r*) and figure 5(*a*–*f*). In the latter, the stresses are shown in the normalization, $\langle\tau\rangle^* = \langle\tau\rangle/(-\langle\partial\bar{P}/\partial x\rangle h) = (A/A_0)\langle\tau\rangle^+$, which appears in (3.10).

The presence of the surface micro-texture gives rise to non-zero mean convective shear stresses, $\langle\tau_{c,xz}\rangle$, in turbulent flow within the 'surface layer', as discussed in Rastegari & Akhavan (2015). These mean flow shear stresses have a common structure for SH longitudinal microgrooves and riblets of a given characteristic size,

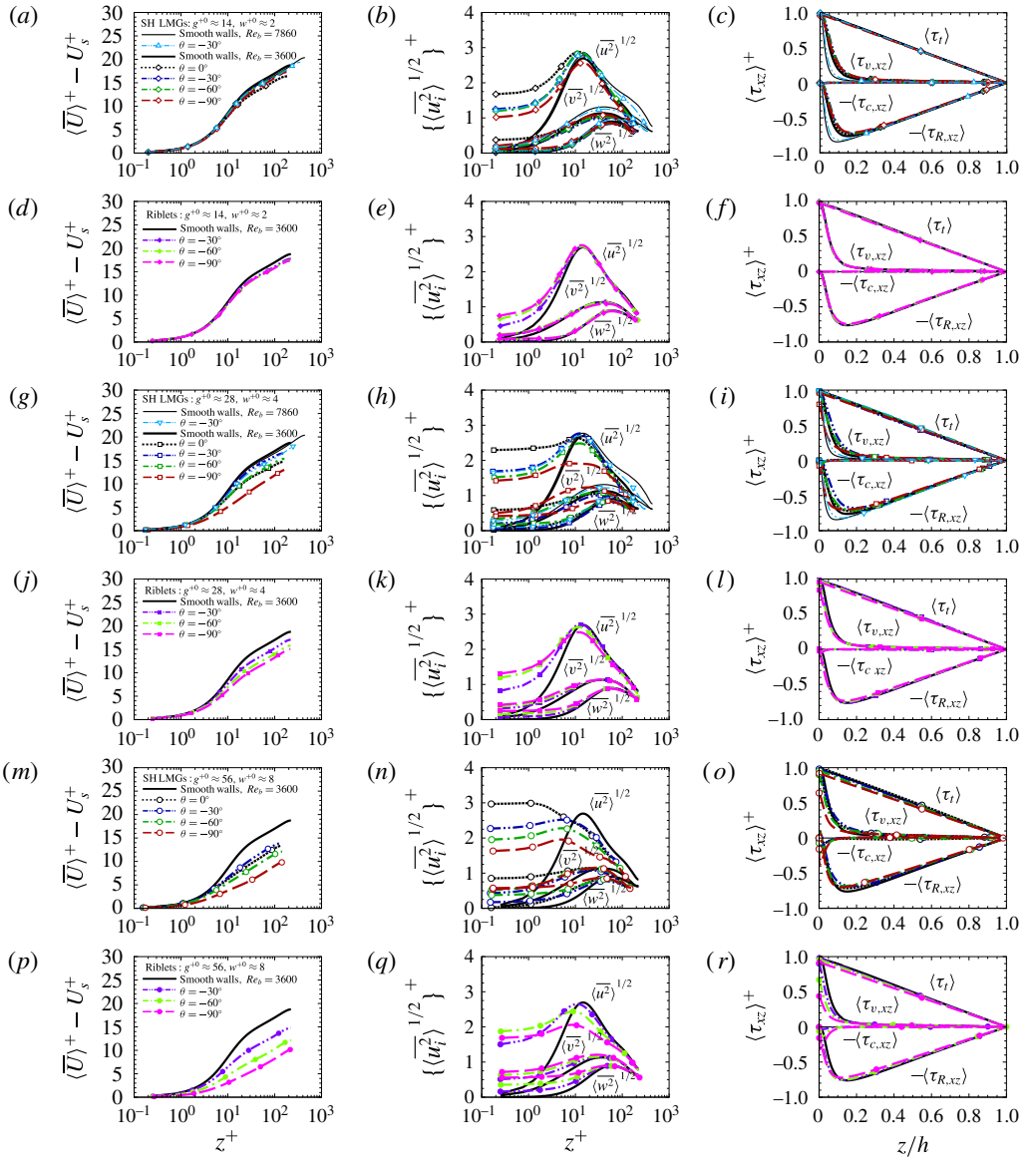

FIGURE 4. Turbulence statistics in channel flow with (*a–c*, *g–i*, *m–o*) SH longitudinal microgrooves (LMGs), and (*d–f*, *j–l*, *p–r*) riblets, compared to channel flow with smooth, no-slip walls: (*a*,*d*,*g*,*j*,*m*,*p*) mean streamwise velocity with the effective wall slip velocity subtracted; (*b*,*e*,*h*,*k*,*n*,*q*) turbulence intensities; (*c*,*f*,*i*,*l*,*o*,*r*) Reynolds shear stress, $\langle \tau_{R,xz} \rangle^+ = -\rho \langle \overline{uw} \rangle^+$, viscous shear stress, $\langle \tau_{v,xz} \rangle^+ = \langle \mu \partial \bar{U} / \partial z \rangle^+$, mean convective stress, $\langle \tau_{c,xz} \rangle^+ = -\rho \langle \bar{U} \bar{W} \rangle^+$, and total shear stress, $\langle \tau_t \rangle^+ = \langle \tau_{R,xz} \rangle^+ + \langle \tau_{v,xz} \rangle^+ + \langle \tau_{c,xz} \rangle^+$.

l_g^+, and always have a drag enhancing contribution to drag reduction, as shown in figures 4(*c*,*f*,*i*,*l*,*o*,*r*), 5(*a*,*d*,*b*,*e*,*c*,*f*) and 3(*b*).

The presence of the surface micro-texture also gives rise to changes in the structure of normalized Reynolds shear stresses, $\langle \tau_{R,xz} \rangle^*$, compared to the base flow, as shown in figure 5. These changes contribute to drag reduction through the $\{DR_{\langle \tau_R \rangle}\}$ term in

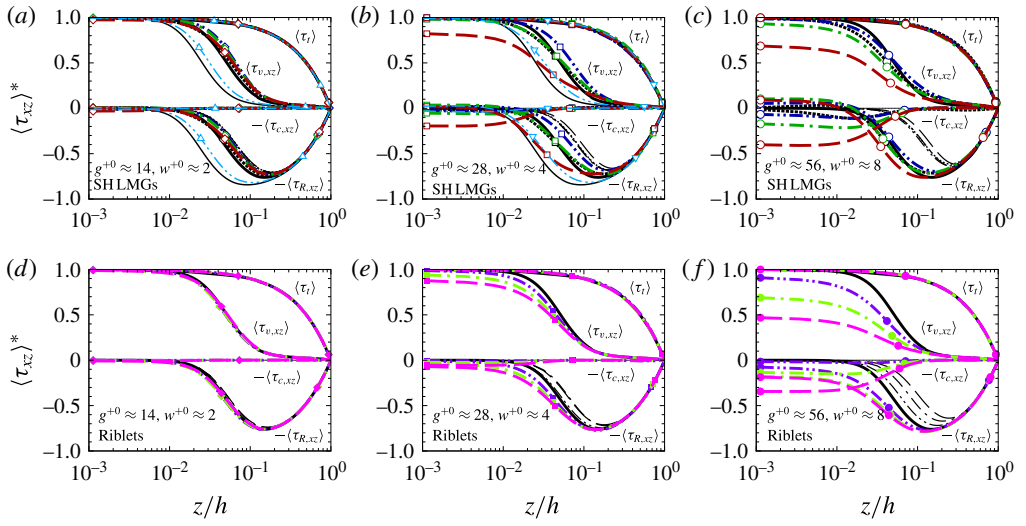

FIGURE 5. Shear stresses, $\langle\tau\rangle^* = \langle\tau\rangle/(-\langle\partial\bar{P}/\partial x\rangle h) = (A/A_0)\langle\tau\rangle^+$, in turbulent channel flow with (*a–c*) SH longitudinal microgrooves, and (*d–f*) riblets, compared to turbulent channel flow with smooth, no-slip walls. ·····, — · · —, — · —, – – –, Reynolds shear stress, $\langle\tau_{R,xz}\rangle^*_{Re_{b_e}}$, in a smooth, no-slip turbulent channel flow at bulk Reynolds number equal to Re_{b_e} of the corresponding SH or riblet case with $\theta = 0°$, $\theta = -30°$, $\theta = -60°$ and $\theta = -90°$ and $Re_b = 3600$, respectively. Other line types as in figure 4.

(3.10), and can be either drag reducing or drag enhancing, as shown in figure 3(*a*). Unlike other examples of drag-reduced turbulent flow, where drag reduction is accompanied by dramatic changes to the normalized Reynolds shear stresses, the changes to $\langle\tau_{R,xz}\rangle^*$ in drag reduction with micro-textured surfaces are subtle, and confined to a thin 'surface layer' of thickness $\sim 2g$, once again confirming that the main mechanism of drag reduction with micro-textured surfaces is surface slip. Figure 5(*a–c*) shows that for all SH longitudinal microgrooves with a microgroove depth $d^+ \lesssim 10.5$, the normalized Reynolds shear stresses, $\langle\tau_{R,xz}\rangle^*$, have a lower magnitude within the surface layer compared to the base flow, giving rise to drag reducing contributions from $\{DR_{\langle\tau_R\rangle}\}$, as observed for these cases in figure 3(*a*). The only SH cases for which $\langle\tau_{R,xz}\rangle^*$ had a higher magnitude within the surface layer compared to the base flow were the SH microgrooves with $g^{+0}\approx 28$ and $g^{+0}\approx 56$ at $\theta = -90°$, for which $d^+ \gtrsim 10.5$, and $\{DR_{\langle\tau_R\rangle}\}$ is, accordingly, drag enhancing. With riblets, on the other hand, $\langle\tau_{R,xz}\rangle^*$ always had a higher magnitude within the surface layer compared to the base flow, as shown in figure 5(*d–f*), giving rise to drag enhancing contributions from $\{DR_{\langle\tau_R\rangle}\}$, as observed for riblets in figure 3(*a*).

Figure 5(*a–f*) also shows the Reynolds shear stresses, $\langle\tau_{R,xz}\rangle^*_{Re_{b_e}}$, which would be obtained in a smooth, no-slip channel flow at a bulk Reynolds number equal to Re_{b_e} of the corresponding SH longitudinal microgroove or riblet case. The differences between these $\langle\tau_{R,xz}\rangle^*_{Re_{b_e}}$ and $\langle\tau_{R,xz}\rangle^*_0$ in the base flow represent the effect of the wall slip velocity, U_s, on the turbulent Reynolds shear stresses, and give rise to the drag reducing contributions from $\{DR_{\langle\tau_R\rangle Re_{b_e}}\}$ observed in figure 3(*c*). Similarly, the differences between $\langle\tau_{R,xz}\rangle^*$ in the flows with micro-textured walls and these $\langle\tau_{R,xz}\rangle^*_{Re_{b_e}}$ represent other modifications to the normalized structure of turbulent shear stresses due to the presence of the surface micro-texture, beyond the effect of U_s, and give

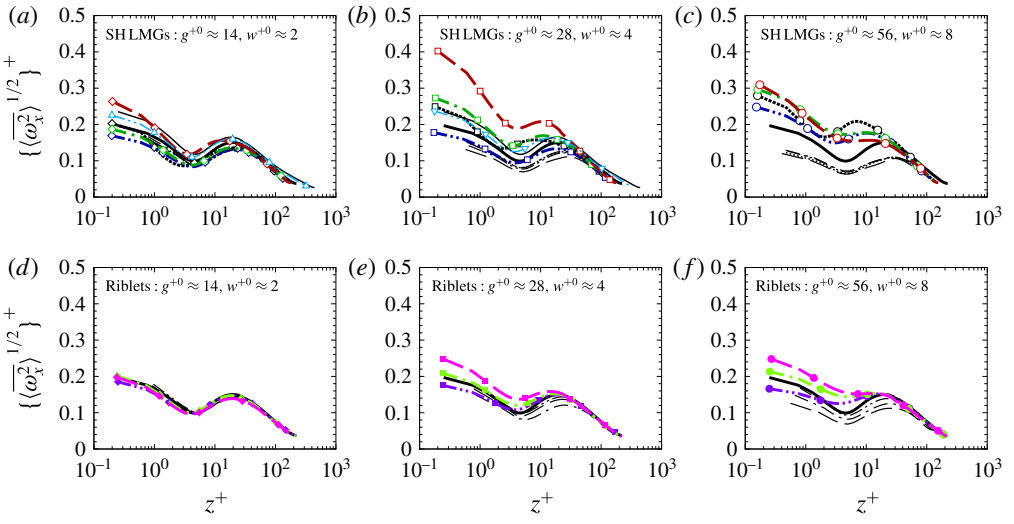

FIGURE 6. Root-mean-square (r.m.s.) streamwise vorticity fluctuations in turbulent channel flow with (*a–c*) SH longitudinal microgrooves, and (*d–f*) riblets, compared to base channel flow with smooth, no-slip walls. ·····, — · · —, — · —, – – –, streamwise r.m.s. vorticity fluctuations, $\{\overline{\langle\omega_x^2\rangle}^{1/2}\}^+_{Re_{b_e}}$, in a smooth, no-slip turbulent channel flow at bulk Reynolds number equal to Re_{b_e} of the corresponding SH or riblet case with $\theta = 0°$, $\theta = -30°$, $\theta = -60°$ and $\theta = -90°$ and $Re_b = 3600$, respectively. Other line types as in figure 4.

rise to the drag enhancing contributions from $\{DR_{\langle\tau_R\rangle_{mod}}\}$ observed in figure 3(*d*). In general, the presence of surface micro-texture has two competing effects on the normalized structure and dynamics of Reynolds shear stresses and near-wall vortical structures: a weakening effect due to establishment of streamwise surface slip, and a strengthening effect due to establishment of spanwise surface slip. The streamwise slip gives rise to the differences between $\langle\tau_{R,xz}\rangle^*_{Re_{b_e}}$ and $\langle\tau_{R,xz}\rangle^*_0$ in the base flow, while the spanwise slip gives rise to the differences between $\langle\tau_{R,xz}\rangle^*$ in the flows with micro-textured walls and $\langle\tau_{R,xz}\rangle^*_{Re_{b_e}}$.

Similar features can also be observed with the near-wall streamwise vortical structures, as shown in figure 6. The presence of streamwise surface slip results in a weakening of the streamwise vorticity fluctuations within the 'surface layer' to the magnitudes shown for $\{\overline{\langle\omega_x^2\rangle}^{1/2}\}^+_{Re_{b_e}}$ in each figure, while the presence of spanwise surface slip strengthens the near-wall streamwise vorticity fluctuations from their $\{\overline{\langle\omega_x^2\rangle}^{1/2}\}^+_{Re_{b_e}}$ values back to magnitudes which can be either smaller or greater than those in the base flow. In general, for SH longitudinal microgrooves of characteristic size $l_g^+ \lesssim 7$ and riblets of characteristic size $l_g^+ \lesssim 8.5$, the magnitudes of $\{\overline{\langle\omega_x^2\rangle}^{1/2}\}^+$ within the 'surface layer' fell below those in the base flow. For a given width, g^{+0}, of the microgrooves in base flow wall units, the lowest and highest magnitudes of $\{\overline{\langle\omega_x^2\rangle}^{1/2}\}^+$ were always observed at $\theta = -30°$ and $\theta = -90°$, respectively, with both SH longitudinal microgrooves and riblets.

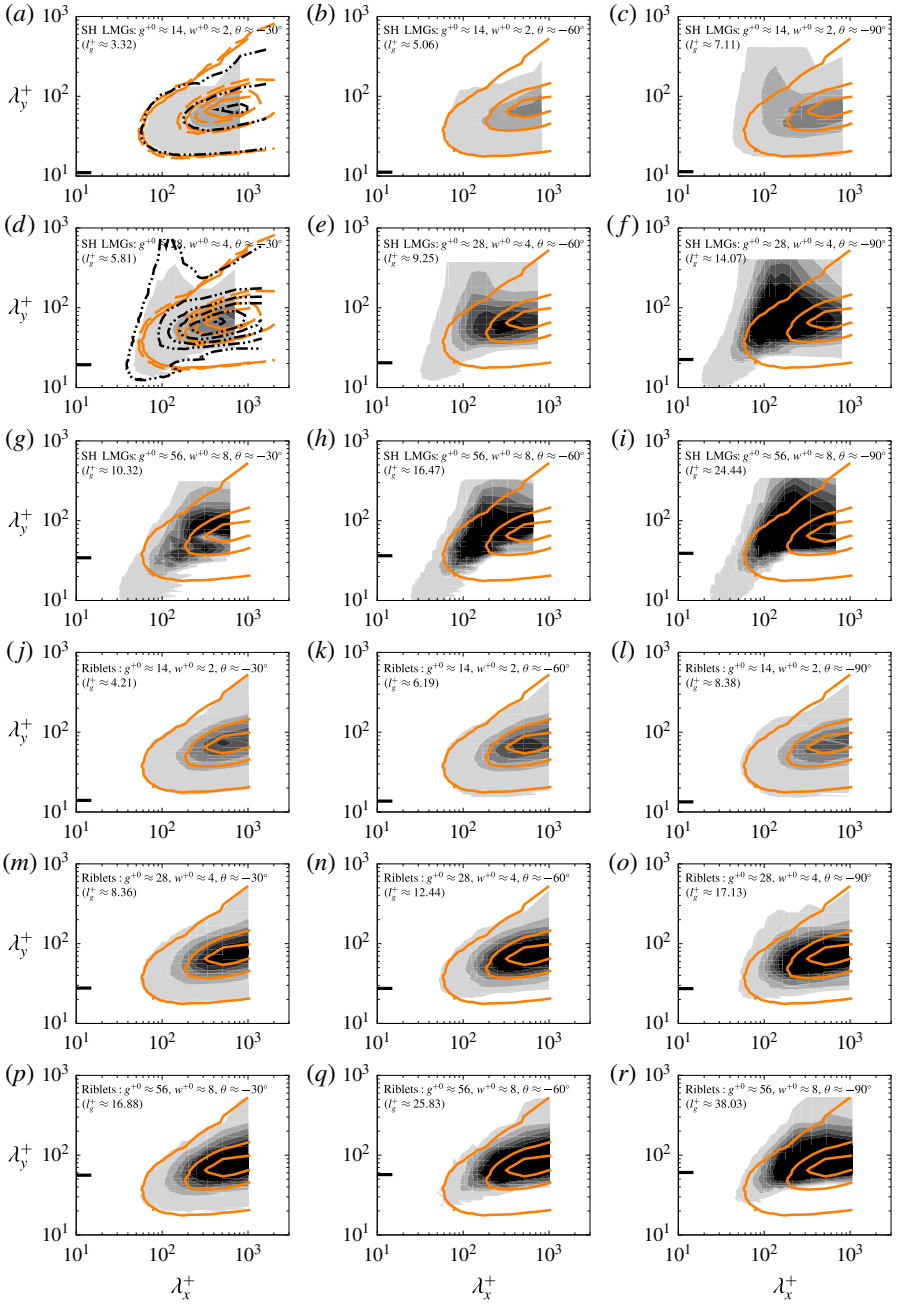

FIGURE 7. Pre-multiplied two-dimensional co-spectra of the Reynolds shear stress, $k_x^+ k_y^+ E_{uw}^+$, at $z^+ \approx 5$, in turbulent channel flow with (*a–i*) SH longitudinal microgrooves, and (*j–r*) riblets, compared to turbulent channel flow with smooth, no-slip walls. Shaded contours correspond to channels with SH longitudinal microgrooves or riblets at $Re_b = 3600$; — · · — (black), contour lines in channels with SH longitudinal microgrooves at $Re_b = 7860$; ——, – – – (orange), contour lines in channels with smooth, no-slip walls at $Re_b = 3600$ and $Re_b = 7860$, respectively. Contour levels at $(0.00025 : 0.01 : 0.05025)$. The tick mark on the left of each plot marks the microgroove width.

4.3. *Role of spanwise rollers*

It has been suggested that the drag enhancing features observed in $\{DR_\varepsilon\}$ and $\{DR_{\langle\tau_R\rangle}\}$ with riblets are caused by the appearance of long spanwise rollers in the region below $z^+ \approx 15$–20, with typical streamwise wavelengths of $\lambda_x^+ \approx 150$, that develop from a two-dimensional Kelvin–Helmholtz–like instability of the mean streamwise flow (Garcia-Mayoral & Jimenez 2011*a*,*b*, 2012). These rollers can be visualized by examining the pre-multiplied, two-dimensional co-spectra of the Reynolds shear stress at a location below $z^+ \approx 15 - 20$. Figure 7 shows these co-spectra at $z^+ \approx 5$ for all the SH longitudinal microgroove and riblet cases investigated in the present study. The presence of spanwise rollers is manifested by accumulation of spectral energy near $\lambda_x^+ \approx 150$ for spanwise wavelengths longer than $\lambda_y^+ \approx 100$, representing elongated structures in the spanwise direction. The strongest evidence of the presence of these spanwise rollers can be seen with SH longitudinal microgrooves in figure 7(*c*–*i*). However, with the exception of the two cases represented by figure 7(*f*,*i*), all other SH cases have a drag reducing contribution from both $\{DR_\varepsilon\}$ and $\{DR_{\langle\tau_R\rangle}\}$. Similarly, with riblets, where there is a drag enhancing contribution from $\{DR_\varepsilon\}$ and $\{DR_{\langle\tau_R\rangle}\}$ for all cases, the evidence of the presence of rollers is fairly weak, and can only be seen in figure 7(*o*,*r*).

These results indicate that there is no correlation between the appearance of spanwise rollers and whether the contributions from $\{DR_\varepsilon\}$ and $\{DR_{\langle\tau_R\rangle}\}$ are drag reducing or drag enhancing. Instead, the appearance of the spanwise rollers seems to be correlated with the depth of the microgrooves and presence of an effective wall slip velocity $U_s^+ \gtrsim 5$–6, with both SH longitudinal microgrooves and riblets.

5. Extrapolation of DNS results to high Reynolds number flows of practical interest

To explore the effect of bulk Reynolds number of the flow on the dynamics reported in § 4, two of the SH simulations, corresponding to longitudinal microgrooves of size $g^{+0} \approx 14$ and $g^{+0} \approx 28$ with $\theta = -30°$, were repeated at $Re_b = 7860$. These simulations correspond to a doubling of the friction Reynolds number of the base flow from $Re_{\tau_0} \approx 222$ at $Re_b = 3600$, to $Re_{\tau_0} \approx 442$ at $Re_b = 7860$. The results of these higher Reynolds number simulations are also shown in table 1 and figures 2–7. The differences between the results at $Re_b = 3600$ and $Re_b = 7860$ are slight, confirming that the lower Reynolds number simulations properly capture the essential features of drag reduction with micro-textured surfaces in turbulent flows at higher Reynolds numbers.

By increasing the Reynolds number of the flow from $Re_b = 3600$ to $Re_b = 7860$, the magnitudes of drag reduction with SH longitudinal microgrooves of size $g^{+0} \approx 14$ and $g^{+0} \approx 28$ with $\theta = -30°$ dropped to $\approx$98 % and $\approx$96 % of their respective values at $Re_b = 3600$, as shown in table 1. In general, as originally demonstrated by Bechert *et al.* (1997) and Spalart & McLean (2011), and discussed in more detail in this section, the drag reduction performance of micro-textured surfaces, with a given geometry and size of the wall micro-texture in wall units, degrades with increasing bulk Reynolds number of the flow, due to the drop in the friction coefficient, C_{f_0}, of the base flow with increasing bulk Reynolds number. The main source of this degradation in drag reduction performance is a drop in the magnitude of $\{DR_{slip}\}$ with increasing bulk Reynolds number. The reason for this drop can be understood by noting that the slip velocity normalized in wall units, U_s^+, remains invariant with the Reynolds number for a given characteristic size of the microgrooves, l_g^+,

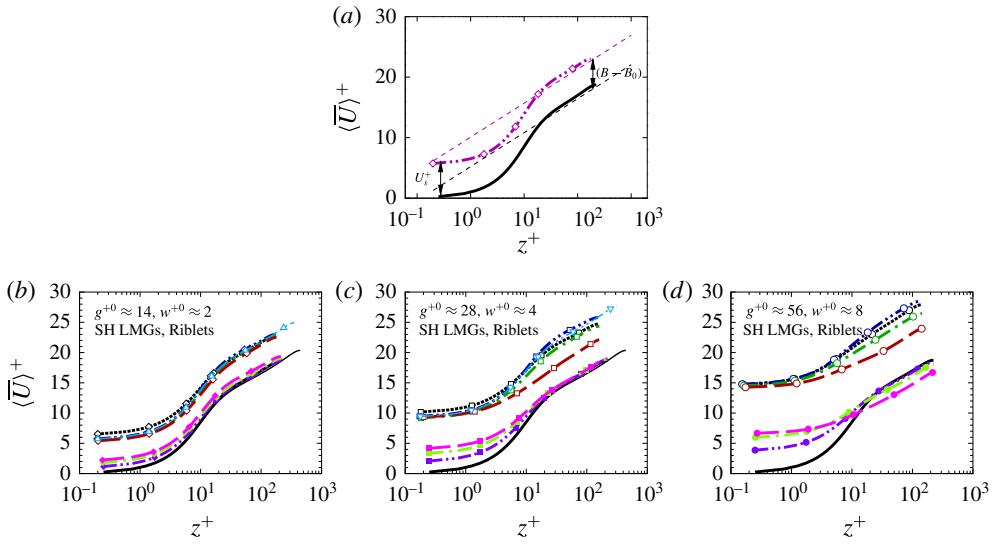

FIGURE 8. Streamwise mean velocity profiles in turbulent channel flow with micro-textured walls compared to turbulent channel flow with smooth, no-slip walls: (*a*) general characteristics of the mean velocity profiles in the presence of micro-textured walls; (*b–d*) mean velocity profiles in turbulent channel flow with SH longitudinal microgrooves or riblets. Line types in (*b–d*) as in figure 4.

as shown in table 1. Consequently, quantities which are proportional to (U_s/U_b), such as $\{DR_{slip}\}$, will experience a degradation with increasing Reynolds number, approximately proportional to the ratios of $\sqrt{C_{f_0}}$ in their respective base flows. In the present study, this effect results in $\{DR_{slip}\}$ values at $Re_b = 7860$ which are 91–92 % of the values as $Re_b = 3600$, which is approximately equal to the ratio of $\sqrt{C_{f_0}}$ in the 'base' flows at $Re_b = 7860$ and $Re_b = 3600$. Part of this drop in drag reduction due to $\{DR_{slip}\}$ is compensated by $\{DR_{Q_g}\}$, which becomes less drag enhancing with increasing bulk Reynolds number of the base flow. In general, $\{DR_{Q_g}\}$ represents a low Reynolds number effect and its magnitude should become negligible at high Reynolds numbers. The percentage of drag reduction arising from $\{DR_\varepsilon\}$ remained approximately unchanged for the two Reynolds numbers investigated in the present study.

Aside from these adjustments to the magnitude of *DR*, the other features of drag-reduced flows at $Re_b = 7860$, including the characteristics of mean velocity profiles, turbulence intensities, Reynolds shear stresses, mean flow shear stresses, streamwise vorticity fluctuations, and two-dimensional co-spectra remained similar to those described for $Re_b = 3600$, as shown in figures 4–7. These findings are consistent with observations by a number of other investigators (Garcia-Mayoral & Jimenez 2012; Park *et al.* 2013; Seo *et al.* 2015), who have also found little effect of Reynolds number on the physics of drag reduction with micro-textured surfaces, and have concluded that the physics deduced from DNS studies at $Re_{\tau_0} \approx 200$ contain the essential features of drag reduction found in higher Reynolds number turbulent flows.

The drag reduction results obtained in DNS can be extended to higher Reynolds number flows of practical interest, using the parameterization of *DR* in terms of

the shift in the intercept of a logarithmic-law representation of the mean velocity profiles, as suggested by Bechert *et al.* (1997) and Spalart & McLean (2011). In this parameterization, the mean velocity profiles in the channel flows with micro-textured walls and in the base channel flow with smooth, no-slip walls are each approximated by logarithmic velocity profiles throughout the cross-section of the channel, as shown in figure 8. These logarithmic profiles are then integrated, and set equal to the bulk velocity, to get

$$\frac{U_b}{u_\tau} = \frac{1}{h}\int_0^h \left(\frac{1}{\kappa}\ln z^+ + B\right)\,\mathrm{d}z = \frac{1}{\kappa}\ln\left(Re_b\sqrt{\frac{C_f}{2}}\right) + \left(B - \frac{1}{\kappa}\right), \tag{5.1}$$

$$\frac{U_{b_0}}{u_{\tau_0}} = \frac{1}{h}\int_0^h \left(\frac{1}{\kappa}\ln z^+ + B_0\right)\,\mathrm{d}z = \frac{1}{\kappa}\ln\left(Re_b\sqrt{\frac{C_{f_0}}{2}}\right) + \left(B_0 - \frac{1}{\kappa}\right), \tag{5.2}$$

where κ is the von Kármán constant, and B and B_0 are the intercepts of logarithmic-law representations of the mean velocity profiles in the channel flow with micro-textured walls and the channel flow with smooth, no-slip walls, respectively, as shown in figure 8(*a*).

Using the definitions $U_b/u_\tau = \sqrt{2/C_f}$ and $U_{b_0}/u_{\tau_0} = \sqrt{2/C_{f_0}}$, (5.1) and (5.2) can be combined to give an expression for $DR = (1 - C_f/C_{f_0})$ as

$$(1 - DR) = \left\{1 + \left[\frac{1}{2\kappa}\ln(1 - DR) + (B - B_0)\right]\sqrt{\frac{C_{f_0}}{2}}\right\}^{-2}. \tag{5.3}$$

Equation (5.3) provides a parameterization of DR in terms of the shift, $(B - B_0)$, of a logarithmic-law representation of the mean velocity profile in the flow with micro-textured walls compared to the base flow. Approximate forms of (5.3), for the limit of low drag reduction, have been earlier derived for riblets (Bechert *et al.* 1997; Spalart & McLean 2011). In this limit, (5.3) can be approximated by

$$DR \approx \frac{(B - B_0)}{\dfrac{1}{2\kappa} + \sqrt{\dfrac{1}{2C_{f_0}}}} \approx (B - B_0)\sqrt{2C_{f_0}}. \tag{5.4}$$

It has been suggested that, in drag reduction with micro-textured surfaces, $(B - B_0)$ is independent of Reynolds number, and only a function of the geometrical parameters of the surface micro-texture in wall units (Clauser 1956; Bechert *et al.* 1997; Spalart & McLean 2011; Garcia-Mayoral & Jimenez 2012). As such, (5.3) can be used to investigate the effect of the bulk Reynolds number of the flow on drag reduction with micro-textured surfaces.

Figure 9(*a*) shows the magnitudes of DR as a function of $(B - B_0)$ from DNS of turbulent channel flow with SH longitudinal microgrooves or riblets in the present study, compared to the predictions of (5.3). The appearance of $\sqrt{C_{f_0}}$ in (5.3) leads to a degradation of DR with increasing bulk Reynolds of the flow. The magnitude of this degradation, as predicted by (5.3), is consistent with the degradation of DR observed in DNS when the Re_b was increased from 3600 to 7860. Figure 9(*a*) also shows the predictions of (5.3) for higher Reynolds number flows of practical interest, up to $Re_b = 7.3 \times 10^8$ ($Re_{\tau_0} \approx 10^6$). It can be seen that, for a given value of $(B - B_0)$,

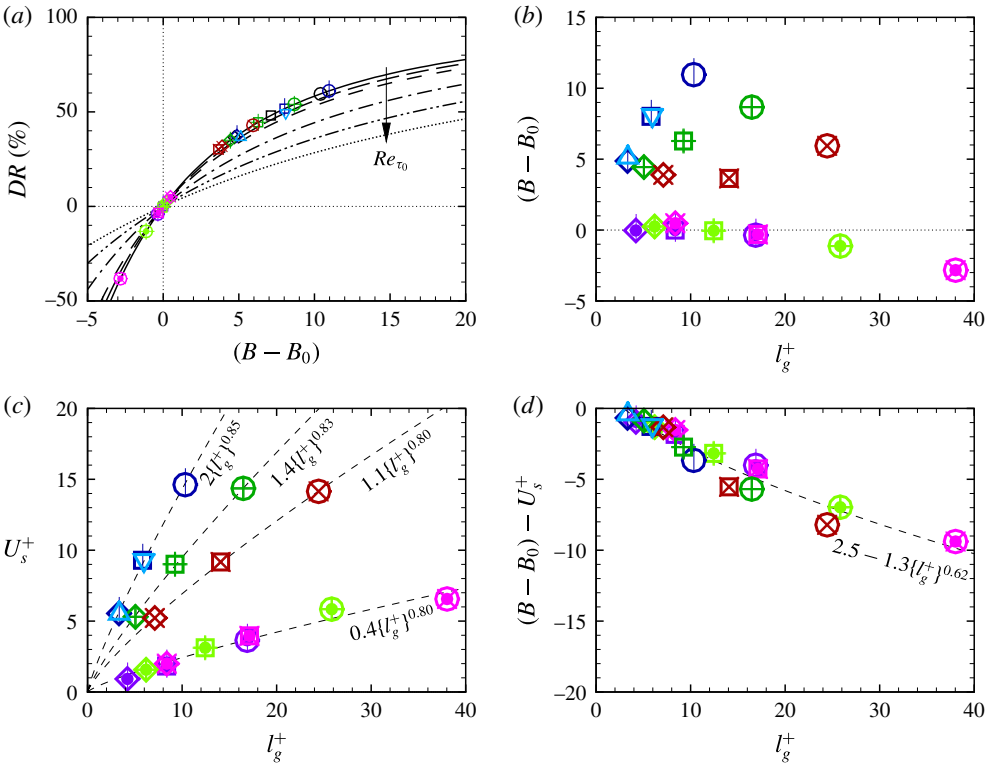

FIGURE 9. Parameterization of DR in turbulent channel flow with SH longitudinal microgrooves or riblets in terms of the shift, $(B-B_0)$, of a logarithmic-law representation of the mean velocity profile and the Reynolds number of the base flow: (*a*) DR as a function of $(B-B_0)$ and the friction Reynolds number of the base flow; (*b*) $(B-B_0)$ as a function of l_g^+; (*c*) average streamwise slip velocity, U_s^+, as a function of l_g^+; (*d*) $\{(B-B_0)-U_s^+\}$ as a function of l_g^+. Line types in (*a*): ——, $Re_b = 3600$ ($Re_{\tau_0} \approx 222$); — —, $Re_b = 7860$ ($Re_{\tau_0} \approx 442$); – – –, $Re_b = 2\times10^4$ ($Re_{\tau_0} \approx 10^3$); — · —, $Re_b = 2.7\times10^5$ ($Re_{\tau_0} \approx 10^4$); — · · —, $Re_b = 3.8\times10^6$ ($Re_{\tau_0} \approx 10^5$); · · · · · ·, $Re_b = 5.3\times10^7$ ($Re_{\tau_0} \approx 10^6$). Symbols as in figure 3.

the drag reduction performance of SH longitudinal microgrooves and riblets degrades considerably with increasing bulk Reynolds number of the flow. Nevertheless, with a proper choice of the surface micro-texture geometry, drag reductions of up to 40–50 % should still be feasible with SH longitudinal microgrooves, assuming the liquid/gas interfaces in SH microgrooves remain stable and do not collapse.

Figure 9(*b*) shows the variation of $(B-B_0)$ with the characteristic size of the microgrooves, l_g^+, from DNS of turbulent channel flow with SH longitudinal microgrooves or riblets in the present study. Good agreement can be seen in the $(B-B_0)$ values at different bulk Reynolds numbers for SH longitudinal microgrooves of size $g^{+0} \approx 14$ and 28 at $\theta = -30°$, confirming the Reynolds number independence of $(B-B_0)$. However, the $(B-B_0)$ values for SH longitudinal microgrooves with different protrusion angles do not collapse and show different trends compared to those for riblets.

To gain a better understanding of the source of these differences, one can decompose $(B - B_0)$ into

$$(B - B_0) = \{U_s^+\} + \{(B - B_0) - U_s^+\}, \tag{5.5}$$

where $\{U_s^+\}$ is the average streamwise slip velocity at the tip of the surface micro-texture, as shown in figure 8, representing all the drag reducing contributions to *DR* arising from streamwise slip, while $\{(B - B_0) - U_s^+\}$ represents all the drag enhancing contributions to *DR* arising from spanwise slip, mean flow shear stresses developed due to the presence of the surface micro-texture and the faction of the flow rate through the surface micro-texture. Figure 9(*c*,*d*) shows the breakdown of $(B - B_0)$ into $\{U_s^+\}$ and $\{(B - B_0) - U_s^+\}$ from DNS of SH longitudinal microgroove and riblets in the present study. With riblets, $\{U_s^+\}$ follows the scaling $U_s^+ \approx 0.4\{l_g^+\}^{0.8}$ for all microgroove depths, while with SH longitudinal microgrooves, it follows scalings which range from $U_s^+ \approx 2.0\{l_g^+\}^{0.85}$ at $\theta = -30°$, to $U_s^+ \approx 1.1\{l_g^+\}^{0.8}$ at $\theta = -90°$, indicating that with increasing protrusion angle, the scaling of $\{U_s^+\}$ with SH longitudinal microgrooves begins to approach that of riblets. The drag enhancing contributions represented by $\{(B - B_0) - U_s^+\}$, however, show a common scaling with both SH longitudinal microgrooves and riblets, as shown in figure 9(*d*), once again indicating that, aside from their magnitudes of streamwise surface slip, SH longitudinal microgrooves and riblets share a common mechanism of drag reduction. The collapse of the data from SH longitudinal microgrooves and riblets in figure 9(*d*) is not as good as the results shown in figures 2(*k*) and 3(*b*,*d*), due to the approximations used in the derivation in (5.3). Nevertheless, the characterization of *DR* in terms of $(B - B_0)$ given by (5.3), combined with the results shown in figure 9, provides a simple method for predicting the magnitude of drag reduction with micro-textured surfaces in high Reynolds number turbulent flows of practical interest.

6. Implications for design of more stable SH surfaces

The presence of a common mechanism of drag reduction with SH longitudinal microgrooves and riblets suggests that the two approaches can be combined synergistically to reduce the pressure loads on SH interfaces, and enhance their longevity and sustainability in turbulent flow environments.

Figure 10(*a–c*) shows the r.m.s. pressure fluctuations in turbulent channel flows with SH longitudinal microgrooves investigated in the present study. The presence of interface curvature at the protrusion angle of $\theta = -30°$ leads to drops of 13 %, 15 % and 28 % in the magnitudes of r.m.s. pressure fluctuations at the wall with microgrooves of size $g^{+0} \approx 14$, 28 and 56, compared to same-size microgrooves with flat SH interfaces, respectively. The drops in instantaneous pressure fluctuations are even more dramatic, as shown in figure 10(*d–g*) for the case $g^{+0} \approx 14$. The instantaneous pressure fluctuations on the micro-textured wall with SH longitudinal microgrooves at $\theta = -30°$ are nearly a factor of two smaller than the micro-textured wall with SH longitudinal microgrooves at $\theta = 0°$.

These results suggest that one can improve the stability of SH surfaces by developing hybrid designs of SH surfaces, in which the SH surface is embedded within the microgrooves of shallow ($\theta = -30°$) scalloped riblets. Indeed, this may be the design adopted by nature in shark scales, which has gone unnoticed to date.

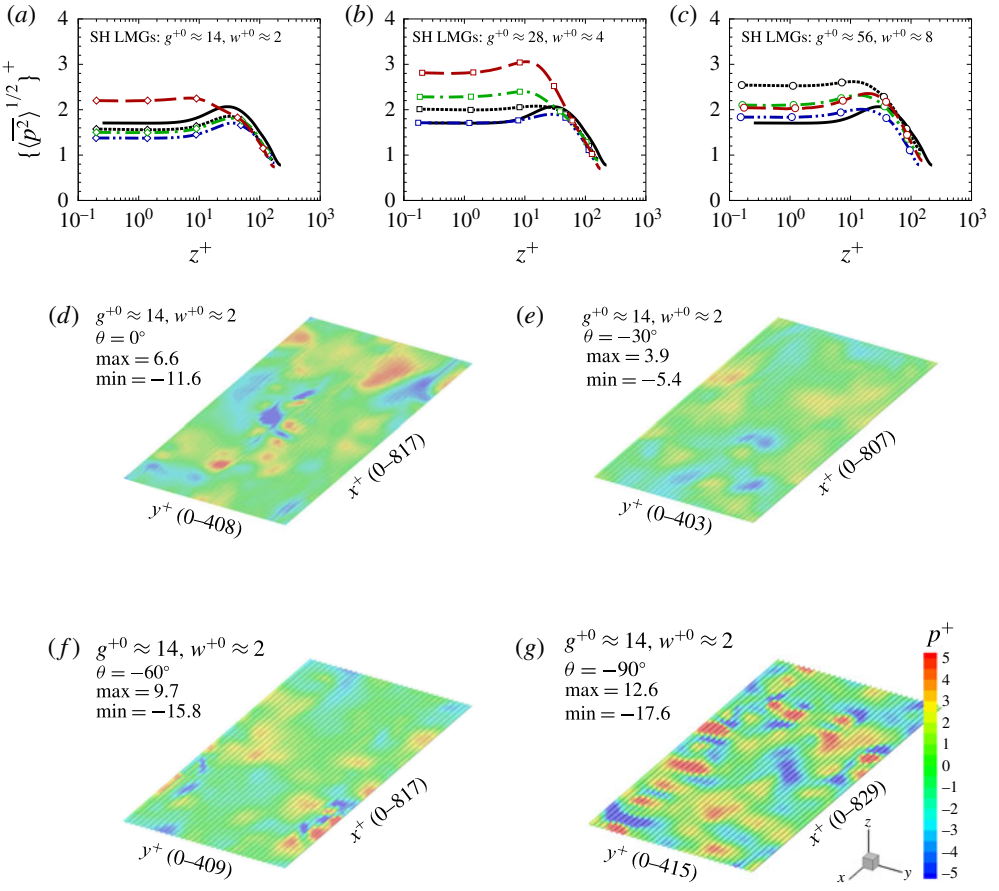

FIGURE 10. Turbulent pressure fluctuations in channel flow with SH longitudinal microgrooves: (*a–c*) r.m.s. turbulent pressure fluctuations; (*d–g*) contour plots of instantaneous turbulent pressure fluctuations on the channel boundaries for $g^{+0} \approx 14$; $w^{+0} \approx 2$ and $\theta = 0°$, $-30°$, $-60°$, $-90°$, respectively. Line types as in figure 4.

7. Summary and conclusions

Skin-friction drag reduction with SH longitudinal microgrooves and riblets has been investigated by mathematical analysis and DNS in channel flow. An exact analytic expression is derived for the magnitude of drag reduction with micro-textured surfaces, which allows the net drag reduction to be decomposed into its constitutive elements. It is shown that in laminar or turbulent channel flow with any SH or riblet micro-texture pattern on the walls, five elements contribute to the net drag reduction: (i) the effective slip velocity at the wall, which augments the bulk velocity and allows a fraction (U_s/U_b) of the flow rate to flow inviscidly; (ii) modifications to the normalized structure of turbulent Reynolds shear stresses due to this augmentation of the bulk velocity by the effective slip velocity at the wall; (iii) other modifications to the normalized structure of turbulent Reynolds shear stresses in the presence of the wall micro-texture; (iv) modifications to the mean flow shear stresses due to the presence of the wall micro-texture; and (v) the flow rate through the wall micro-texture.

Comparison to DNS results in turbulent channel flow at $Re_b = 3600$ ($Re_{\tau_0} \approx 222$) and $Re_b = 7860$ ($Re_{\tau_0} \approx 442$) shows that SH longitudinal microgrooves and riblets share a common mechanism of drag reduction, in which 100 % of the drag reduction arises from effects (i) and (ii), namely, the effective slip velocity at the wall, and modifications to the normalized structure of turbulent Reynolds shear stresses due the presence of this effective slip velocity. All other modifications to the normalized structure of turbulent Reynolds shear stresses and the structure of the mean flow shear stresses due to the presence of the wall micro-texture, as well as the effect of the flow rate through the wall micro-texture, are drag enhancing, and follow common scalings for SH longitudinal microgrooves and riblets when expressed as a function of the characteristic size of the wall micro-texture, $l_g^+ = \sqrt{A_G^+}$.

It is shown that DNS studies at $Re_{\tau_0} \approx 200$ properly represent the physics of drag reduction with micro-textured surfaces at higher Reynolds numbers. Extrapolation of drag reduction data from DNS to high Reynolds number flows of practical interest is discussed. It is shown that, for a given geometry and size of the surface micro-texture in wall units, there is significant degradation in the drag reduction performance of micro-textured surfaces with increasing Reynolds number of the flow.

Curved SH interfaces with small protrusion angle ($\theta = -30°$) are shown to reduce the r.m.s. and instantaneous pressure fluctuations on the SH interface compared to flat SH surfaces. This suggests that the longevity of SH surfaces in turbulent flow environments may be improved by using hybrid designs, in which the SH surface is embedded within the microgrooves of shallow ($\theta = -30°$) scalloped riblets.

Acknowledgements

This work was supported by an unrestricted grant from the M. R. Prince Foundation, and NSF XSEDE Allocation TG-CTS070067N. This support is gratefully acknowledged. The study has greatly benefited from suggestions by the anonymous referees. We thank the referees for this anonymous contribution.

Appendix A. Verification of numerical methods

A number of numerical tests were performed to verify the accuracy of the lattice Boltzmann methods and adequacy of the grid resolutions and domain sizes employed in the present study. These tests include (i) comparisons of lattice Boltzmann DNS to pseudo-spectral DNS in turbulent channel flow with smooth, no-slip walls; (ii) verification of grid independence of the results, by comparisons of lattice Boltzmann DNS results on successively refined grids in turbulent channel flows with SH longitudinal microgrooves with flat SH interfaces; (iii) verification of adequacy of the domain size, by comparisons of lattice Boltzmann DNS in small and large domain turbulent channel flows with SH longitudinal microgrooves with flat SH interfaces; and (iv) verification of curved interface boundary conditions, by comparisons of lattice Boltzmann DNS results to numerical simulations of Wang *et al.* (2014) in laminar channel flows with SH longitudinal microgrooves and curved SH interfaces at various interface protrusion angles.

A.1. *Comparisons to pseudo-spectral DNS in turbulent channel flow with smooth walls*

All the simulations reported in the present study were performed using standard D3Q19, single relaxation time lattice Boltzmann methods (Succi 2001), with grid

embedding (Lagrava *et al.* 2012) employed in the near-wall region, between the domain boundaries and the buffer layer ($z^{+0} \approx 30$), to improve the accuracy of the computations near the micro-textured walls.

The accuracy of the lattice Boltzmann DNS code in turbulent flow with smooth, no-slip walls was assessed by comparing its results, both with and without grid embedding, to pseudo-spectral DNS in turbulent channel flow. The studies were performed in channels of size $5h \times 2.5h \times 2h$ in the streamwise, spanwise and wall-normal directions, respectively. A constant flow rate was maintained in the channel during the course of all the simulations, corresponding to a bulk Reynolds number of $Re_b = 3600$. The lattice Boltzmann DNS without grid embedding was performed using uniform grid spacings of $\Delta^{+0} \approx 2$, which is the standard recommended resolution for DNS of turbulent wall-bounded flows with lattice Boltzmann methods (Lammers *et al.* 2006). The lattice Boltzmann DNS with grid embedding was performed with a grid refinement ratio of $GR = 4$, employed in the region between the domain boundaries and the buffer layer ($z^{+0} \approx 30$), resulting in grid spacings of $\Delta_f^{+0} \approx 0.5$ for $z^{+0} \lesssim 30$, and $\Delta_c^{+0} \approx 2$ for $z^{+0} \gtrsim 30$, as shown in figure 1(*b*). The pseudo-spectral DNS was performed using uniform Fourier grids of size $\Delta_x^{+0} \approx 8$ and $\Delta_y^{+0} \approx 4$ in the streamwise and spanwise directions, respectively, and non-uniform Chebyshev grids of size $0.07 \lesssim \Delta_z^{+0} \lesssim 4.5$ in the wall-normal direction.

The skin-friction coefficients predicted by lattice Boltzmann DNS, with and without grid embedding, were within 0.1 and 1 % of the values predicted by pseudo-spectral DNS, respectively, as shown in table 2. Similarly, the normalized profiles of mean streamwise velocities, turbulence intensities and Reynolds shear stresses predicted by lattice Boltzmann DNS, with and without grid embedding, were within 1 and 4 % of the results obtained from pseudo-spectral DNS, respectively, as shown in figure 11(*a–c*). These results indicate that the higher resolutions provided by grid embedding are not essential for lattice Boltzmann DNS in turbulent channel flows with smooth, no-slip walls. However, the higher resolutions offered by grid embedding in the near-wall region improve the accuracy of the simulations.

A.2. *Need for grid embedding in flows with micro-textured surfaces and verification of grid independence of the results*

With micro-textured surfaces, however, grid embedding becomes essential for obtaining accurate results. To demonstrate the need for grid embedding and verify the grid independence of the results, simulations both with and without grid embedding were performed in turbulent channel flows with SH longitudinal microgrooves of size $g^{+0} \approx 28$, $w^{+0} \approx 4$ and $g^{+0} \approx 56$, $w^{+0} \approx 8$, at interface protrusion angle of $\theta = 0°$, as shown in table 2. These simulations were also performed in channels of size $5h \times 2.5h \times 2h$ in the streamwise, spanwise and wall-normal directions, respectively, at a bulk Reynolds number of $Re_b = 3600$. The simulations without grid embedding were performed with uniform grid spacings of $\Delta^{+0} \approx 2$ throughout the domain. The simulations with grid embedding were performed with a grid refinement ratio of $GR = 4$ within the region $z^+ \lesssim 30$, and two different sets of grid resolutions, corresponding to $\Delta_f^{+0} \approx 0.5$, $\Delta_c^{+0} \approx 2$, and $\Delta_f^{+0} \approx 1$, $\Delta_c^{+0} \approx 4$, respectively, to verify the grid independence of the results.

The skin-friction coefficients obtained with grid spacings of $\Delta_f^{+0} \approx 1$, $\Delta_c^{+0} \approx 4$, were within 1.2 % and 1.7 % of those obtained with $\Delta_f^{+0} \approx 0.5$, $\Delta_c^{+0} \approx 2$, for flows with SH longitudinal microgrooves of size $g^{+0} \approx 28$, $w^{+0} \approx 4$ and $g^{+0} \approx 56$, $w^{+0} \approx 8$, respectively, as reported in table 2. Similarly, the normalized profiles of mean

https://doi.org/10.1017/jfm.2017.865 Published online by Cambridge University Press

Case	Δ_x^{+0}	Δ_y^{+0}	Δ_z^{+0}	g^{+0}	w^{+0}	θ	$L_x \times L_y \times L_z$	$C_f \times 10^3$
PS, smooth walls	8.1	4.4	$0.07 - 4.5$	—	—	—	$5h \times 2.5h \times 2h$	7.610
LB, smooth walls	0.5 & 2.0	0.5 & 2.0	0.5 & 2.0	—	—	—	$5h \times 2.5h \times 2h$	7.603
LB, smooth walls	2.0	2.0	2.0	—	—	—	$5h \times 2.5h \times 2h$	7.686
LB, smooth walls (L)	2.0	2.0	2.0	—	—	—	$20h \times 10h \times 2h$	7.765
LB, SH walls	0.5 & 2.0	0.5 & 2.0	0.5 & 2.0	28	4	0°	$5h \times 2.5h \times 2h$	3.946
LB, SH walls	1.0 & 4.0	1.0 & 4.0	1.0 & 4.0	28	4	0°	$5h \times 2.5h \times 2h$	3.901
LB, SH walls (L)	1.0 & 4.0	1.0 & 4.0	1.0 & 4.0	28	4	0°	$20h \times 10h \times 2h$	3.923
LB, SH walls	2.0	2.0	2.0	28	4	0°	$5h \times 2.5h \times 2h$	3.697
LB, SH walls (L)	2.0	2.0	2.0	28	4	0°	$20h \times 10h \times 2h$	3.743
LB, SH walls	0.5 & 2.0	0.5 & 2.0	0.5 & 2.0	56	8	0°	$5h \times 2.5h \times 2h$	3.079
LB, SH walls	1.0 & 4.0	1.0 & 4.0	1.0 & 4.0	56	8	0°	$5h \times 2.5h \times 2h$	3.025
LB, SH walls (L)	1.0 & 4.0	1.0 & 4.0	1.0 & 4.0	56	8	0°	$20h \times 10h \times 2h$	3.002
LB, SH walls	2.0	2.0	2.0	56	8	0°	$5h \times 2.5h \times 2h$	2.805
LB, SH walls (L)	2.0	2.0	2.0	56	8	0°	$20h \times 10h \times 2h$	2.819

TABLE 2. Summary of the simulations performed to assess the accuracy of numerical methods, grid independence of the results, and adequacy of the domain size. All tests were performed in turbulent channel flow at $Re_b = 3600$. PS and LB denote pseudo-spectral and lattice Boltzmann methods, respectively.

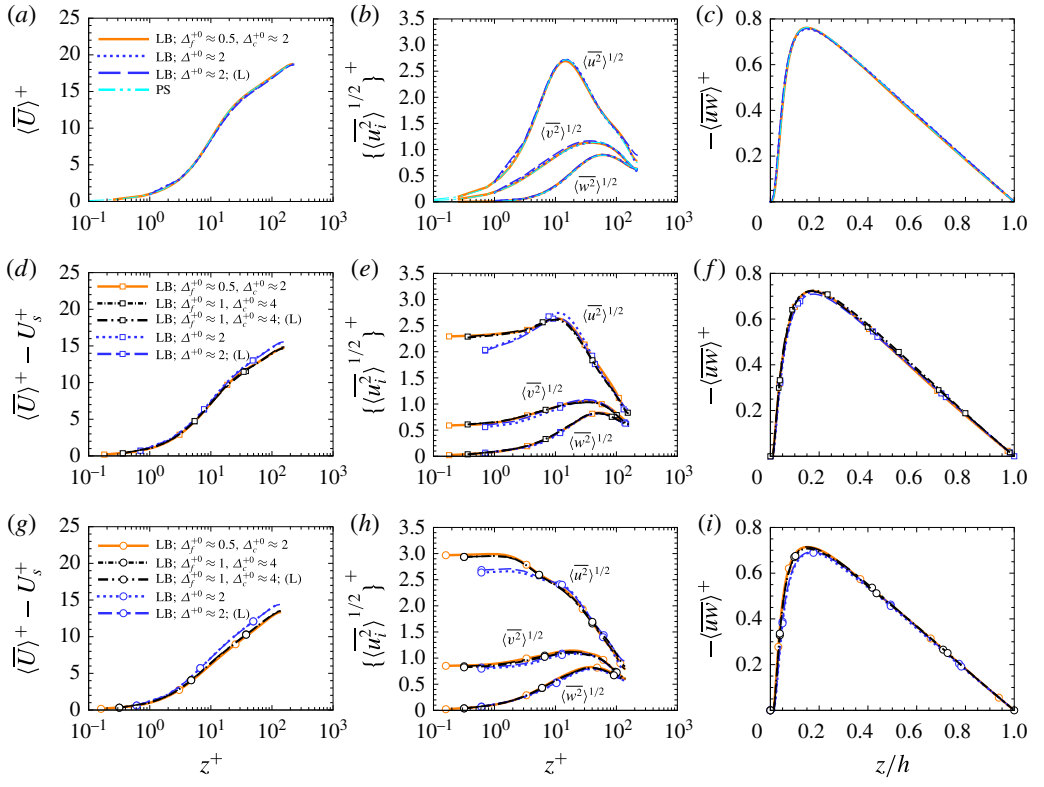

FIGURE 11. Effect of grid resolution and domain size on turbulence statistics in (*a–c*) turbulent channel flow with smooth, no-slip walls; (*d–f*) turbulent channel flow with SH longitudinal microgrooves of size $g^{+0} \approx 28$, $w^{+0} \approx 4$ at protrusion angle of $\theta = 0°$; (*g–i*) turbulent channel flow with SH longitudinal microgrooves of size $g^{+0} \approx 56$, $w^{+0} \approx 8$ at protrusion angle of $\theta = 0°$: (*a*,*d*,*g*) mean velocity profiles; (*b*,*e*,*h*) turbulence intensities; (*c*,*f*,*i*) Reynolds shear stresses. (L) denotes simulations performed in large domains.

streamwise velocities, turbulence intensities and Reynolds shear stresses obtained with grid spacings of $\Delta_f^{+0} \approx 1$, $\Delta_c^{+0} \approx 4$, were within 2.5 % of the results obtained with $\Delta_f^{+0} \approx 0.5$, $\Delta_c^{+0} \approx 2$, as shown in figure 11(*d–i*). These results demonstrate the grid independence of the results and adequacy of the grid spacings of $\Delta_f^{+0} \approx 0.5$, $\Delta_c^{+0} \approx 2$ employed in all the simulations in the present study.

Without grid embedding, the predicted skin-friction coefficients differed from the values obtained with grid embedding, and grid spacings of $\Delta_f^{+0} \approx 0.5$, $\Delta_c^{+0} \approx 2$, by up to 10 %, as reported in table 2, while the normalized profiles of mean streamwise velocities, turbulence intensities and Reynolds shear stresses differed by up to 13 %, as shown in figure 11(*d–i*). These deviations show that grid spacings of $\Delta^{+0} \approx 2$ do not provide an adequate grid resolution for lattice Boltzmann DNS of turbulent flows with a wall micro-texture.

The need for grid embedding in the presence of a surface micro-texture arises from the formation of sharp shear layers between the slip and no-slip regions at the tip of the surface microgrooves. These shear layers lead to sharp velocity gradients in the spanwise direction near the surface micro-texture. The effect of these gradients extends away from the walls to distances of the order of the width of the microgrooves. A fine grid, with grid spacings of the order of $\Delta^{+0} \approx 0.5$, is necessary to resolve the gradients

near the micro-textured walls. Beyond a distance of $z^{+0} \approx 30$, however, the spanwise gradients have weakened to the point that grid spacings of the order of $\Delta^{+0} \approx 2$ can adequately resolve the weakened gradients.

These features can be verified by examining the one-dimensional energy spectra of turbulent velocity fluctuations, $E^{+}_{\alpha\alpha}$, as shown in figure 12. When a coarse grid, of size $\Delta^{+0} \approx 2$, is used near the micro-textured walls, the inadequate grid resolution within the region $z^{+0} \lesssim 30$ leads to a pile up of turbulence kinetic energy in the one-dimensional energy spectra for spanwise wavenumbers $k^{+}_{y} \gtrsim 0.3$, as shown in figure 12(*e*,*f*). Increasing the grid resolution to $\Delta^{+0}_{f} \approx 0.5$ in this region, by employing grid embedding, resolves these issues and leads to disappearance of the energy pile-up, as seen in figure 12(*e*,*f*). Beyond a distance of $z^{+0} \approx 30$ from the walls, however, no pile up of energy is observed with $\Delta^{+0} \approx 2$, as seen in figure 12(*k*,*l*), indicating that grid spacings of $\Delta^{+0}_{c} \approx 2$ provide adequate resolution for $z^{+0} \gtrsim 30$.

A.3. *Effect of domain size*

The simulations reported in this study were all performed in channels of size $5h \times 2.5h \times 2h$ in the streamwise, spanwise and wall-normal directions, respectively. To assess the effect of domain size on the results, the simulations in base turbulent channel flow with smooth, no-slip walls, and in turbulent channel flows with SH longitudinal microgrooves of size $g^{+0} \approx 28$, $w^{+0} \approx 4$ and $g^{+0} \approx 56$, $w^{+0} \approx 8$, with interface protrusion angle of $\theta = 0°$, were repeated in channels of size $20h \times 10h \times 2h$, as reported in table 2. A bulk Reynolds number of $Re_b = 3600$ was maintained in the channel in all of these simulations. To reduce the cost of the computations, all the large domain simulations were performed either without grid embedding, at grid spacings of $\Delta^{+0} \approx 2$, or with grid embedding, at grid spacings of $\Delta^{+0}_{f} \approx 1$ and $\Delta^{+0}_{c} \approx 4$, as shown in table 2.

Comparison of DNS results in the small and large domains shows that the size of the domain has a negligible effect on the resulting skin-friction coefficients and turbulence statistics. The skin-friction coefficients obtained in the large domains were all within 0.5–1.2 % of the values obtained in the small domains with the same grid spacings, as shown in table 2. Similarly, the turbulence statistics and spectra in the large and small domains were in good agreement, as shown in figures 11 and 12. The largest differences in the turbulence statistics were observed in the streamwise turbulence intensities in the out layer ($z^{+} \gtrsim 100$), where the values from the large domains could be higher than those in the small domains by up to 10 %, as shown in figure 11(*b*,*e*,*h*).

Figure 13 shows the two-point correlations of turbulent velocity fluctuations, $R_{\alpha\alpha}$, in the large and small domains, at $z^{+} \approx 5$ and $z/h = 0.8$. In the large domains, the two-point correlations drop to zero at a separation of one half the domain lengths in both the near-wall region, $z^{+} \approx 5$, and the core, $z/h = 0.8$. The two-point correlations in the smaller domains follow the trends in the larger domains, and drop to sufficiently low values at a separation of one half their domain lengths to ensure that the turbulence statistics are not affected, except for minor differences in the core region, as seen in figure 11. These results indicate the adequacy of the smaller domain size, employed in the present study.

A.4. *Tests in laminar SH channel flow with curved SH interfaces*

The accuracy of lattice Boltzmann DNS in dealing with curved liquid/gas SH interfaces was verified through comparisons of lattice Boltzmann DNS results, both

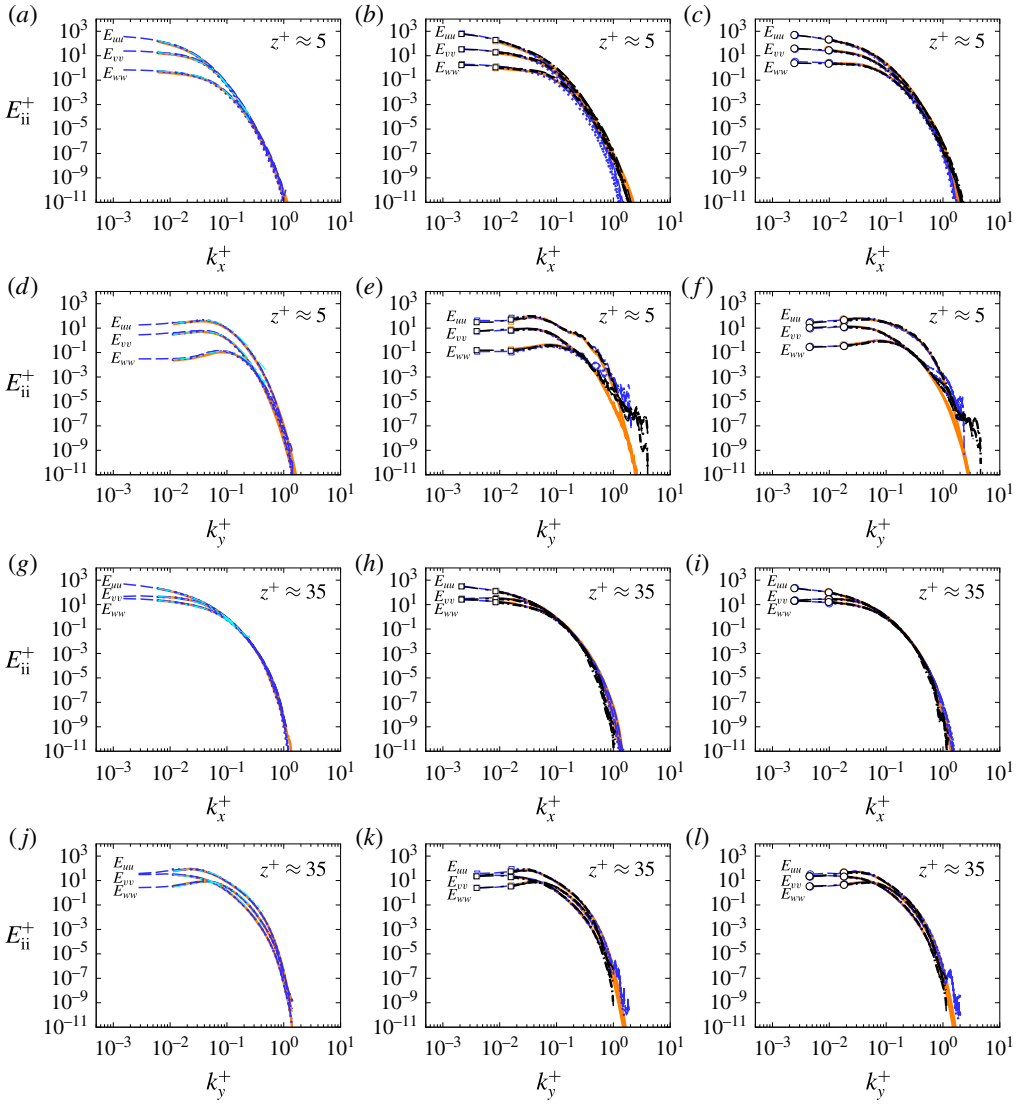

FIGURE 12. Effect of grid resolution and domain size on one-dimensional energy spectra in (*a*,*d*,*g*,*j*) turbulent channel flow with smooth, no-slip walls; (*b*,*e*,*h*,*k*) turbulent channel flow with SH longitudinal microgrooves of size $g^{+0} \approx 28$, $w^{+0} \approx 4$ at protrusion angle of $\theta = 0°$; (*c*,*f*,*i*,*l*) turbulent channel flow with SH longitudinal microgrooves of size $g^{+0} \approx 56$, $w^{+0} \approx 8$ at protrusion angle of $\theta = 0°$. Line types as in figure 11.

with and without grid embedding, with results from numerical simulations of Wang *et al.* (2014), performed using finite-element methods, in laminar channel flows with SH longitudinal microgrooves on the walls. In both studies, the liquid/gas interfaces in the SH longitudinal microgrooves were modelled as static, curved, shear-free boundaries, with the shape of the interface obtained from the solution of the Young–Laplace equation. The lattice Boltzmann simulations were performed in laminar channel flows at a bulk Reynolds number of $Re_b = 150$, with SH longitudinal microgrooves of size $(g + w)/h = 0.196$ and $g/w = 1$ on both walls, to match the geometric parameters of the longitudinal microgrooves in the simulations of

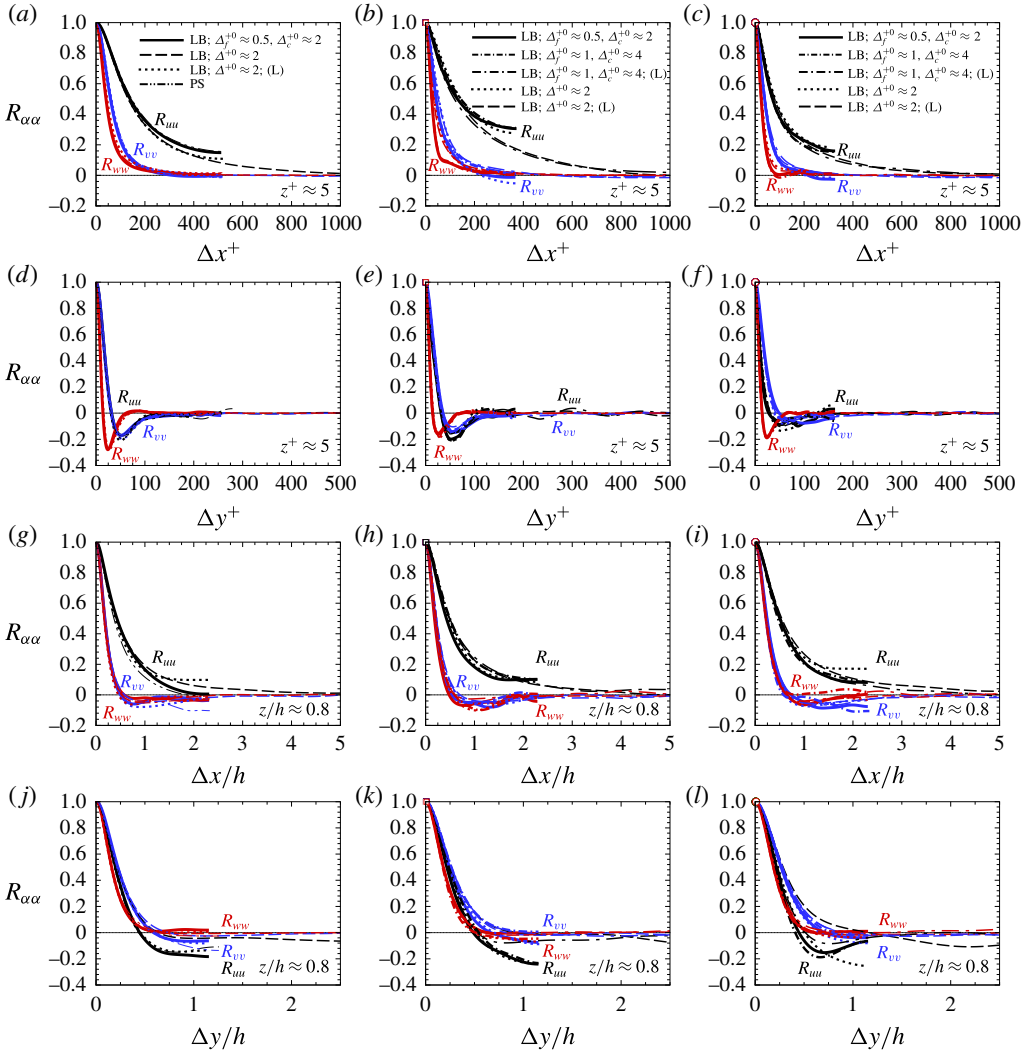

FIGURE 13. Effect of grid resolution and domain size on two-point correlations of velocity fluctuations in (*a*,*d*,*g*,*j*) turbulent channel flow with smooth, no-slip walls; (*b*,*e*,*h*,*k*) turbulent channel flow with SH longitudinal microgrooves of size $g^{+0} \approx 28$, $w^{+0} \approx 4$ at protrusion angle of $\theta = 0°$; (*c*,*f*,*i*,*l*) turbulent channel flow with SH longitudinal microgrooves of size $g^{+0} \approx 56$, $w^{+0} \approx 8$ at protrusion angle of $\theta = 0°$. (L) Denotes simulations performed in large domains.

Wang *et al.* (2014). Static interface protrusion angles of $\theta = 0°$, $-30°$, $-60°$, $-90°$, corresponding to interface curvatures of $\kappa = 0.0$, 1.0, 1.732, 2.0 were investigated. The lattice Boltzmann simulations without grid embedding were performed at grid resolutions of $\Delta/g = 1/32$ and $\Delta/g = 1/64$. The lattice Boltzmann simulations with grid embedding were performed with a grid refinement ratio of $GR = \Delta_c/\Delta_f = 4$, and grid resolutions of $\Delta_f/g = 1/32$ and $\Delta_f/g = 1/64$, where the grid-embedding region extended from the domain boundaries to the tip of the longitudinal microgrooves. Figure 14 shows the resulting slip lengths, L_s/h, and slip velocities, U_s/U_{b0}, computed by lattice Boltzmann DNS, compared to the results of Wang *et al.* (2014). The results

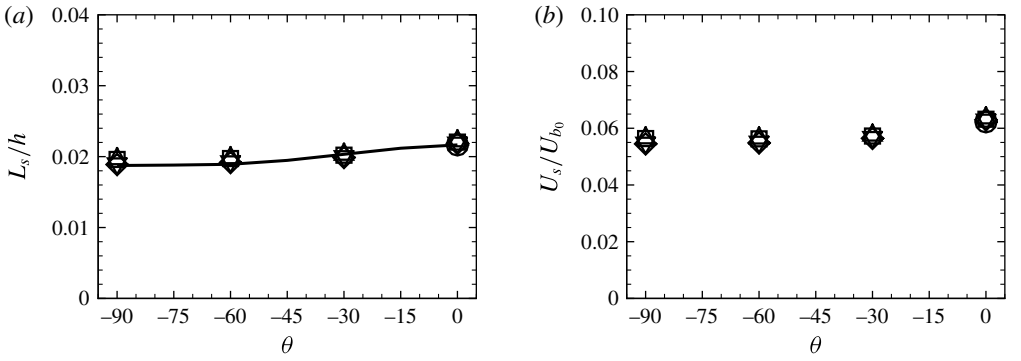

FIGURE 14. Verification of lattice Boltzmann DNS in laminar channel flow with SH longitudinal microgrooves and curved liquid/gas interfaces: (*a*) L_s/h; (*b*) U_s/U_{b_0}. △, ▽, DNS without grid embedding at $\Delta/g = 1/32$ and $\Delta/g = 1/64$, respectively. □, ◇, DNS with $GR = 4$ grid embedding at $\Delta_f/g = 1/32$ and $\Delta_f/g = 1/64$, respectively. ○, analytical solution of Philip (1972); ——, numerical simulations of Wang *et al.* (2014). All simulations performed at $Re_b = 150$ in channels with SH longitudinal microgrooves of size $(g + w)/h = 0.196$ and $g/w = 1$ on both walls.

at different grid resolutions, both with and without grid embedding, are seen to be in agreement with each other and with the results reported by Wang *et al.* (2014), demonstrating grid independence and accuracy of the results. Based on these studies, all the simulations reported in this work were performed with grid-embedding lattice Boltzmann DNS, with grids of size $1/112 \leqslant \Delta_f/g \leqslant 1/28$ and $\Delta_f^{+0} \approx 0.5$ on the fine grid, and a $GR = \Delta_c/\Delta_f = 4$ elsewhere, to ensure that both the dynamics of the flow near the curved boundaries and the turbulence dynamics are properly resolved.

REFERENCES

BECHERT, D. W. & BARTENWERFER, M. 1989 The viscous flow on surfaces with longitudinal ribs. *J. Fluid Mech.* **206**, 105–129.

BECHERT, D. W., BRUSE, M., HAGE, W., VAN DER HOEVEN, J. G. T. & HOPPE, G. 1997 Experiments on drag-reducing surfaces and their optimization with an adjustable geometry. *J. Fluid Mech.* **338**, 59–87.

BUSHNELL, D. & HEFNER, J. N. 1990 Viscous drag reduction in boundary layers. In *Progress in Astronautics and Aeronautics* (ed. D. Bushnell & J. N. Hefner), vol. 123. AIAA.

CHA, T., YI, J. W., MOON, M., LEE, K. & KIM, H. 2010 Nanoscale patterning of microtextured surfaces to control superhydrophobic robustness. *Langmuir* **26**, 8319–8326.

CHECCO, A., OCKO, B. M., RHAMN, A., BLACK, C. T., TASINKEVYCH, M., GIACOMELLO, A. & DIETRICH, S. 2014 Collapse and reversibility of the superhydrophobic state on nanotextured surfaces. *Phys. Rev. Lett.* **112**, 216101.

CHOI, H., MOIN, P. & KIM, J. 1993 Direct numerical simulation of turbulent flow over riblets. *J. Fluid Mech.* **255**, 503–539.

CHU, D. C. & KARNIADAKIS, G. E. 1993 A direct numerical simulation of laminar and turbulent flow over riblet-mounted surfaces. *J. Fluid Mech.* **250**, 1–42.

CLAUSER, F. H. 1956 The turbulent boundary layer. *Adv. Appl. Mech.* **4**, 1–51.

CROWDY, D. 2016 Analytical formulae for longitudinal slip lengths over unidirectional superhydrophobic surfaces with curved menisci. *J. Fluid Mech.* **791**, R7.

DEAN, R. D. 1978 Reynolds number dependence of skin friction and other bulk flow variables in two dimensional rectangular duct flow. *Trans. ASME J. Fluids Engng* **100**, 215–223.

FENG, L., LI, S., LI, Y., LI, H., ZHNG, L., ZHAI, J., SONG, Y., LIU, B., JIANG, L. & ZHU, D. 2002 Superhydrophobic surfaces: from natural to artificial. *Adv. Mater.* **14**, 1857–1860.

FUKAGATA, K., IWAMOTO, K. & KASAGI, N. 2002 Contribution of Reynolds stress distribution to the skin-friction in wall-bounded flows. *Phys. Fluids* **14**, L73–L76.

FUKAGATA, K., KASAGI, N. & KOUMOUTSAKOS, P. 2006 A theoretical prediction of friction drag reduction in turbulent flow by superhydrophobic surfaces. *Phys. Fluids* **18**, 051703.

GARCIA-MAYORAL, R. & JIMENEZ, J. 2011*a* Hydrodynamic stability and breakdown of the viscous regime over riblets. *J. Fluid Mech.* **678**, 317–347.

GARCIA-MAYORAL, R. & JIMENEZ, J. 2011*b* Drag reduction by riblets. *Phil. Trans. R. Soc. Lond.* A **369**, 1412–1427.

GARCIA-MAYORAL, R. & JIMENEZ, J. 2012 Scaling of turbulent structures in riblet channels up to $\mathrm{Re}_\tau = 550$. *Phys. Fluids* **24**, 105101.

DE GENNES, P., BROCHARD-WYART, F. & QUÉRÉ, D. 2002 *Capillarity and Wetting Phenomena: Drops, Bubbles, Pearls, Waves*. Springer.

GINZBURG, I. & STEINER, K. 2003 Lattice Boltzmann model for free-surface flow and its application to filling process in casting. *J. Comput. Phys.* **185**, 61–99.

GINZBURG, I., VERHAEGHE, F. & D'HUMIÈRES, D. 2008 Two-relaxation-time lattice Boltzmann scheme: About parametrization, velocity, pressure and mixed boundary conditions. *Commun. Comput. Phys.* **3**, 427–478.

GOLDSTEIN, D. B., HANDLER, R. & SIROVICH, L. 1995 Direct numerical simulation of turbulent flow over a modeled riblet covered surface. *J. Fluid Mech.* **302**, 333–376.

GOLDSTEIN, D. B. & TUAN, T.-C. 1998 Secondary flow induced by riblets. *J. Fluid Mech.* **363**, 115–151.

JELLY, T. O., JUNG, S. Y. & ZAKI, T. A. 2014 Turbulence and skin friction modification in channel flow with streamwise-aligned superhydrophobic surface texture. *Phys. Fluids* **26**, 095102.

JUNG, T., CHOI, H. & KIM, J. 2016 Effects of the air layer of an idealized superhydrophobic surface on the slip length and skin-friction drag. *J. Fluid Mech.* **790**, R1.

KARATAY, E., TSAI, P. A. & LAMMERTINK, R. G. 2013*a* Rate of gas absorption on a slippery bubble mattress. *Soft Matt.* **9**, 11098–11106.

KARATAY, E., HAASE, A. S., VISSER, C. W., SUN, C., LOHSE, D., TSAI, P. A. & LAMMERTINK, R. G. 2013*b* Control of slippage with tunable bubble mattresses. *Proc. Natl Acad. Sci. USA* **110**, 8422–8426.

KWON, Y., PATNAKAR, N., CHOI, J. & LEE, J. 2009 Design of surface hierarchy for extreme hydrophobicity. *Langmuir* **25**, 6129–6136.

LAGRAVA, D., MALASPINAS, O., LATT, J. & CHOPARD, B. 2012 Advances in multi-domain lattice Boltzmann grid refinement. *J. Comput. Phys.* **231**, 4808–4822.

LAMMERS, P., BERONOV, K. N., VOLKERT, R., BRENNER, G. & DURST, F. 2006 Lattice BGK direct numerical simulation of fully developed turbulence in incompressible plane channel flow. *Comput. Fluids* **35**, 1137–1153.

LEE, C. & KIM, C.-J. 2009 Maximizing the giant liquid slip on superhydrophobic microstructures by nanostructuring their sidewalls. *Langmuir* **25**, 12812–12818.

LEE, C. & KIM, C.-J. 2011 Underwater restoration and retention of gases on superhydrophobic surfaces for drag reduction. *Phys. Rev. Lett.* **106**, 014502.

LUCHINI, P., MANZO, F. & POZZI, A. 1991 Resistance of a grooved surface to parallel flow and cross-flow. *J. Fluid Mech.* **228**, 87–109.

MARTEL, M., PEROT, J. B. & ROTHSTEIN, J. P. 2009 Direct numerical simulations of turbulent flows over superhydrophobic surfaces. *J. Fluid Mech.* **620**, 31–41.

MARTEL, M. B., ROTHSTEIN, J. P. & PEROT, J. B. 2010 An analysis of superhydrophobic turbulent drag reduction mechanisms using direct numerical simulation. *Phys. Fluids* **22**, 065102.

MIN, T. & KIM, J. 2004 Effect of superhydrophobic surfaces on skin-friction drag. *Phys. Fluids* **16**, L55.

NISHINO, T., MEGURO, M., NAKAMAE, K., MATSUSHITA, M. & UEDA, Y. 1999 The lowest surface free energy based on CF3 alignment. *Langmuir* **15**, 4321–4323.

OU, J. & ROTHSTEIN, J. P. 2005 Direct velocity measurements of the flow past drag reducing ultrahydrophobic surfaces. *Phys. Fluids* **17**, 103606.

PARK, H., PARK, H. & KIM, J. 2013 A numerical study of the effects of superhydrophobic surface on skin-friction drag in turbulent channel flow. *Phys. Fluids* **25**, 110815.

PARK, H., SUN, G. & KIM, C.-J. 2014 Superhydrophobic turbulent drag reduction as a function of surface grating parameters. *J. Fluid Mech.* **747**, 722–734.

PEET, Y. & SAGAUT, P. 2009 Theoretical prediction of turbulent skin friction on geometrically complex surfaces. *Phys. Fluids* **21**, 105105.

PHILIP, J. R. 1972 Flows satisfying mixed no-slip and no-shear conditions. *Z. Angew. Math. Phys.* **23**, 353–372.

RASTEGARI, A. & AKHAVAN, R. 2013 Lattice Boltzmann simulations of drag reduction by superhydrophobic surfaces. In *Proceedings 14th European Turbulence Conference, 1-4 September, Lyon, France*.

RASTEGARI, A. & AKHAVAN, R. 2015 On the mechanism of turbulent drag reduction with superhydrophobic surfaces. *J. Fluid Mech.* **773**, R4.

RATHGEN, H. & MUGEL, F. 2010 Microscopic shape and contact angle measurement at a superhydrophobic surface. *Faraday Discuss.* **146**, 49–56.

ROSENBERG, B. J., VAN BUREN, T., FU, M. K. & SMITS, A. J. 2016 Turbulent drag reduction over air- and liquid- impregnated surfaces. *Phys. Fluids* **28**, 015103.

ROTHSTEIN, J. P. 2010 Slip on superhydrophobic surfaces. *Annu. Rev. Fluid Mech.* **42**, 89–109.

SBRAGAGLIA, M. & PROSPERETTI, A. 2007 A note on the effective slip properties for microchannel flows with ultrahydrophobic surfaces. *Phys. Fluids* **19**, 043603.

SCHELLENBERGER, F., ENCINAS, N., VOLLMER, D. & BUTT, H. 2016 How water advances on superhydrophobic surfaces. *Phys. Rev. Lett.* **116**, 096101.

SEO, J., GARCIA-MAYORAL, R. & MANI, A. 2015 Pressure fluctuations and interfacial robustness in turbulent flows over superhydrophobic surfaces. *J. Fluid Mech.* **783**, 448–473.

SEO, J. & MANI, A. 2016 On the scaling of the slip velocity in turbulent flows over superhydrophobic surfaces. *Phys. Fluids* **28**, 025110.

SPALART, P. R. & MCLEAN, J. D. 2011 Drag reduction: enticing turbulence, and then an industry. *Phil. Trans. R. Soc. Lond.* A **369**, 1556–1569.

STEINBERGER, A., COTTIN-BIZONNE, C., KLEIMANN, P. & CHARLAIX, E. 2007 High friction on a bubble mattress. *Nat. Mater.* **6**, 665–668.

SUCCI, S. 2001 *The Lattice Boltzmann Equation for Fluid Dynamics and Beyond*. Oxford University Press.

TSAI, P., PETERS, A. M., PIRAT, C., WESSLING, M., LAMMERTINK, R. G. H. & LOHSE, D. 2009 Quantifying effective slip length over micropatterned hydrophobic surfaces. *Phys. Fluids* **21**, 112002.

TÜRK, S., DASCHIEL, G., STROH, A., HASEGAWA, Y. & FROHNAPFEL, B. 2014 Turbulent flow over superhydrophobic surfaces with streamwise grooves. *J. Fluid Mech.* **747**, 186–217.

WALSH, M. J. 1980 Drag characteristics of V-groove and transverse curvature riblets. In *Viscous Flow Drag Reduction* (ed. G. R. Hough), Progress in Astronautics and Aeronautics, vol. 72, pp. 168–184. AIAA.

WALSH, M. J. 1982 Turbulent boundary layer drag reduction using riblets. *AIAA Paper* 82-0169.

WALSH, M. J. 1990 Riblets. In *Viscous Drag Reduction in Boundary Layers* (ed. D. Bushnell & J. Hefner), Progress in Astronautics and Aeronautics, vol. 123, pp. 203–259. AIAA.

WANG, Z., KORATKAR, N., CI, L. & AJAYAN, P. M. 2007 Combined micro-/nanoscale surface roughness for enhanced hydrophobic stability in carbon nanotube arrays. *Appl. Phys. Lett.* **90**, 143117.

WANG, L. P., TEO, C. J. & KHOO, B. C. 2014 Effects of interface deformation on flow through microtubes containing superhydrophobic surfaces with longitudinal ribs and grooves. *Microfluid Nanofluid* **16**, 225–236.

WONG, T. S., KANG, S. H., TANG, S. K. Y., SMYTHE, E. J., HATTON, B. D., GRINTHAL, A. & AIZENBERG, J. 2011 Bioinspired self-repairing slippery surfaces with pressure-stable omniphobicity. *Nature* **477**, 443–447.